About chemical Trends in Transition Metal Complexes

Über chemische Trends in Übergangsmetallkomplexen

Doctoral Thesis

Dissertation zur Erlangung des Doktorgrades
Dr. rer. nat.

Max-Planck-Institut für Kohlenforschung

Fakultät für Chemie
Universität Duisburg-Essen

Julian David Rolfes
Master of Science

Dannenrod/Vlotho/Dangast/Mülheim a. d. Ruhr/Essen, Germany
December 2020

The present work was carried out in the research groups of

PROF. DR. TOBIAS RITTER & PROF. DR. FRANK NEESE

under the supervision of

DR. MAURICE VAN GASTEL

from October 2016 to December 2020 at the
MAX-PLANCK-INSTITUT FÜR KOHLENFORSCHUNG
in Mülheim a. d. Ruhr.

DOI: 10.17185/duepublico/74234
URN: urn:nbn:de:hbz:464-20210427-134012-1

1st Examiner: Prof. Dr. Frank Neese
2nd Examiner: Dr. Maurice van Gastel

Date of Disputation: 6th April, 2021

„What we observe is not nature itself,
but nature exposed to our method of questioning.“

WERNER HEISENBERG

Abstract

The present doctoral thesis developed around the objective to generate a bench-stable electrophilic fluorinating reagent (like Selectfluor[1]) from inorganic fluoride as fluorine source. In contrast to the preceding Master's thesis,[1] this thesis does not focus on the synthesis and analysis of potential complexes to catalyze the aforementioned reaction, but rather on some of the theoretical vacancies that deter us as a scientific community from understanding what to take care of in order to successfully design such a reaction.

This thesis presents another fraction of this groundwork like the analysis of an electrophilic fluorination reaction mechanism from a high-valent palladium fluoride complex, the non-existence of a potential "Fluoro Wall" (the respective fluoro-analogon of the Oxo Wall), the generation of a novel all-electron basis set to accurately calculate relativistic properties of fifth period elements, and of course the parallel developments in computational catalyst design for the oxidative activation of fluoride.

Zusammenfassung

Die vorliegende Doktorarbeit entwickelte sich um das Ziel, ein "tischstabiles"[2] elektrophiles Fluorierungsreagenz (wie Selectfluor) aus anorganischem Fluorid als Fluorquelle zu synthetisieren. Im Gegensatz zur vorhergehenden Masterarbeit[1] konzentriert sich diese Arbeit nicht auf die Synthese und Analyse potentieller Komplexe zur Katalyse der oben erwähnten Reaktion, sondern auf einige der offenen theoretischen Fragestellungen, die uns als wissenschaftliche Gemeinschaft davon abhalten zu verstehen, worauf wir achten müssen, um eine solche Reaktion erfolgreich zu gestalten.

In dieser Arbeit wird ein weiterer Bruchteil dieser Grundlagenarbeiten vorgestellt, wie die Analyse eines elektrophilen Fluorierungsreaktionsmechanismus aus einem hochvalenten Palladiumfluoridkomplex, die Nichtexistenz der „Fluoro Wall"(das entsprechende Fluor-Analogon zur Oxo Wall), die Generierung eines neuartigen Vollelektronenbasissatzes zur genauen Berechnung der relativistischen Eigenschaften von Elementen der fünften Periode und natürlich die parallelen Entwicklungen bei dem computergestützten Entwurf von Katalysatoren für die oxidative Aktivierung von Fluorid.

[1] Within this thesis, the term "F-TEDA" is regularly used to describe the Selectfluor dication, and the term "TEDA" (derived from "**T**etra**e**thylene**d**i**a**mine", synonymous for the DABCO backbone of the Selectfluor structure) for the corresponding defluorinated cation.

[2] „Tischstabil"in diesem Zusammenhang bedeutet, dass der betrettende Stoff ohne besondere Vorkehrungen auf einem Labortisch gelagert werden kann.

Acknowledgements

First, I want to thank PROF. DR. FRANK NEESE for giving me the opportunity to join his research group, for his support and for the beautiful freedom regarding my research projects. I honestly could not have asked for a better supervisor in any respect.

Just in the same way, I have to thank DR. MAURICE VAN GASTEL for his supervision, his helpful advises and for taking so much care of me.

I also thank PROF. DR. TOBIAS RITTER for his support and his supervision up to and during the initial phase of my doctral studies. I can not put into words how much I took out of that time.

For the helpful advises and inspiring discussions, but mostly for their friendship I thank SAMIRA SPEICHER, GEORGI STOYCHEV, ZACHARY MATHE, NICO SPILLER, DR. DIMITRIOS PANTAZIS, and DR. GIOVANNI BISTONI.

I thank the NEESE group as well as the teams of the MAX-PLANCK-INSTITUT FÜR KOHLENFORSCHUNG, the MAX PLANCK PHDNET, MPQUEER, the MAX PLANCK SUSTAINABILITY NETWORK, and the MENTAL HEALTH COLLECTIVE OF THE MAX PLANCK SOCIETY for their supportive work environment as well as for having and meeting all the beautiful experiences and people during the last four years.

I dedicate this thesis to my incredible and supportive family (including those I've conciously chosen to be part of it)[3] for all they have done for me. I am nothing without you. This thesis belongs to all of us.

[3] If you read this thesis for correction, definitely consider yourself part of it!

Contents

List of Figures

List of Schemes

Abbrevations

AO	atomic orbital
CC	Coupled Cluster
cf.	confer
CI	Configuration Interaction
CPCM	Conductor-like Polarizable Continuum Model
D	double substitutions
DFT	Density Functional Theory
DLPNO	Domain-based Local Pair Natural Orbital
e. g.	for example (*exempli gratia*)
ECP	Effective Core Potential
F-TEDA	Selectfluor dication (IUPAC: 1-chloromethyl-4-fluoro-1,4-diazabicyclo[2.2.2]octane dication)
GGA	Generalized Gradient Approximation
GTO	GAUSSIAN-type orbitals
HF	HARTREE-FOCK
HOMO	highest occupied molecular orbital
i. e.	that is (*it est*)
incl.	including
LDA	Local Density Approximation
LUMO	lowest unoccupied molecular orbital
MO	molecular orbital
PES	Potential Energy Surface
PET	Positron Emission Tomography
PP	pseudopotential
QRO	quasi-restricted orbital
RI	Resolution of Identity Approximation
S	single substitutions
SARC	Segmented All-Electron Relativistically Contracted
SCF	self-consistent field
SET	single-electron transfer
SOMO	singly occupied molecular orbital

SPP	Spin Polarization Parameter
STO	SLATER-type orbital
T	triple substitutions
TEDA	1-chloromethyl-1,4-diazabicyclo[2.2.2]octane cation
UCO	unrestricted corresponding orbitals
ZPE	zero-point vibrational energy

1 Introduction

The present work focuses on the theoretical evaluation of experimentally observable trends in transition metal complexes. A vast majority of this work deals with computational analyses of reactivity patterns of late transition metal fluoride complexes with a focus on and around high-valent monofluoride complexes of group 10 elements (Ni, Pd, Pt).

In this first chapter, the chemical and methodological groundwork is reviewed, before the present research objective and methodology are described in more detail in the next. In chapter 3, the scientific advances[2]–[4] of my research are presented and contextualized, before the general "Train of Thought" of the studies, on which this doctoral thesis is grounded, is discussed in some more detail. The thesis is finally summarized in chapter 4.

1.1 Preface

This thesis is supposed to comprehend the scientific advances I contributed to during the last four years. However, it would be totally inaccurate to boil down my doctoral phase to my scientific advances only. Looking back, this phase is probably also the time of my life – at least so far – I grew the most not only as a scientist, but also as a person. This is why I decided to append not only my scientific, "academic publications", but also what I call my "other publications" (at least the ones that were published in written form) from this time: to start this thesis as a person[4] *and* to end it as such.

I hope you enjoy reading it.

[4] As opposed to the pure and dry function of a scientist with the aspiration of (pseudo-)objectivity.

1.2 Chemical Groundwork

Chemically, the work presented here builds on two major fundaments: The first one is the concept of the so-called "Oxo Wall" and the second is the recent advance in synthetic and catalytic applications of (high-valent) late transition metal fluoride complexes, especially palladium fluorides:

1.2.1 The Oxo Wall[5]

The Oxo Wall is a widely known and accepted concept among the inorganic chemical community.[5] It states the instability of six-coordinate tetragonal oxo complexes with metals beyond group 8.

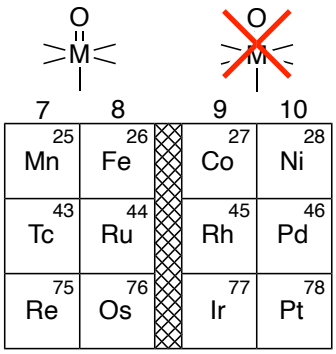

Figure 1: Depiction of the Oxo Wall.

While transition metal oxo complexes are a prominent motif in biological oxidation processes,[6],[7] the concept of the Oxo Wall dates back to 1962 where BALLHAUSEN and GRAY developed a molecular orbital energy level scheme that correctly described the electronic structure of the vanadyl ion.[8] The description of chromyl and molybdenyl ions followed shortly after, where the metal oxo interaction was represented as a triple bond for the first time.[9]

This notion is based on elementary molecular orbital considerations in which the bond order is deduced by subtracting the number of electrons in antibonding orbitals of a given bond from the number of electrons in the bonding counterparts of these orbitals and divide the result by two.[10] For example, in the six-coordinate tetragonal oxo complex $Mo(V)OCl_5^{2-}$ the single d electron is found in the nonbonding d_{xy} orbital, leaving the two other d orbitals of t_{2g} symmetry (d_{xz} and d_{yz}) amenable to π interactions with the $p_{x/y}$ orbitals from the oxo ligand on the z axis. A total of six electrons are present in the two bonding π-orbitals and the bonding σ-orbital (interaction between oxo p_z and metal d_{d^2} orbital) while all antibonding counterparts are empty, thus leaving a metal-oxo triple bond.

The theoretical concept of the Oxo Wall – as stated by GRAY and WINKLER: "Complexes with tetragonal symmetry can have no more than 5 d electrons and still retain some MO multiple

[5] This subchapter is copied from the Manuscript "Where Is the Fluoro Wall?: A Quantum Chemical Investigation"[3] that will be presented and discussed in the course of this work.

bonding. In the absence of π-bonding to the metal, the oxo will be extremely basic and unstable with respect to protonation or attack by electrophiles."[5] – is also supported by a large array of experimental investigations.[11]–[13] While oxo compounds are known with transition metals beyond the Oxo Wall[14], [15] with well-characterized electronic structure,[16] these do not violate the concept of the Oxo Wall because they are not of tetragonal symmetry. Claims that exceptions have been found[17] were later retracted and as such, 'the "Oxo Wall" stands.'[18]

1.2.2 (High-Valent) Late Transition Metal Fluorides

Transition metal fluorides are known and used for many decades.[19], [20] They are readily accessed via oxidative C–F bond activation,[21] nucleophilic fluorination[22] or oxidative electrophilic fluorination.[23] Despite the fact that the range of natural organofluorine compounds is very limited,[24] fluorinated molecules are of particularly high interest in materials, agrochemicals and pharmaceuticals.[25]–[31] Especially the emergence of Positron Emmission Tomography (PET)[32] and the concomitant need for late-stage fluorination methodologies to effectively include the radioisotope ^{18}F into organic molecules gave rise to a totally new form of reaction design, the so called "radiofluorination".[33]–[37]

Especially important for this work are those late transition metal fluoro complexes that would violate a potential Fluoro Wall, the fluoro equivalent to the well documented Oxo (cf. 1) and Nitro Walls[38], [39]; in contrast to the latter elements, even perfectly octahedral hexafluoride complexes beyond the potential Fluoro Wall are well documented.[40] Furthermore, fluoro complexes with six-coordinate tetragonal geometry for a significant part of the second half of the transition metals are often hypothesized (with varying degrees of evidence) as active intermediates in catalytic fluorination reactions.[25]

A big step forward was the experimental revelation that, shown with a cationic palladium fluoride,[41] high-valent late transition metal fluoride complexes can in principle serve as S_N2 "fluoronium" (F^+) donors. This means, starting from fluoride, the compound mentioned above is able to perform an *umpolung*-like reaction[42] on fluorine, the most electronegative element of the periodic table. Interestingly, it has been shown that this S_N2-type "fluoronium" transfer proceeds through an unusual SET/fluoride transfer/SET mechanism:[43] instead of transferring an F^+, after all, the fluorine is transferred in the form of an F^-, enclosed by two individual single-electron transfers (SET) from the nucleophile to the palladium. Hence, this reaction type is more accurately described as an oxidative fluori**d**ation.

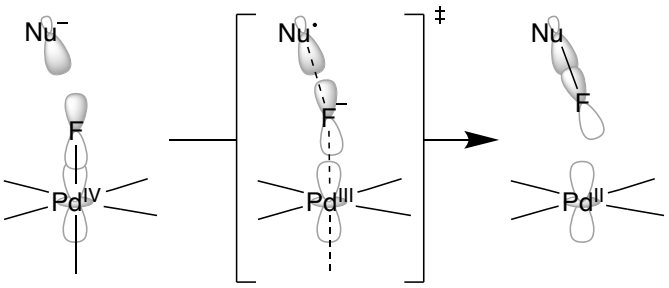

Scheme 1: S_N2-type fluorination reaction, following an unusual SET/fluoride transfer/SET mechanism.

1.3 Methodological Groundwork[6]

As the present work is mostly theoretical, the following part seeks to introduce the basic theories behind the field of computational chemistry. The main objective of computational chemistry is to accurately describe intrinsic properties of a chemical system by means of quantum mechanical methodology. There are different strategies to approach the quantum physical description of a given chemical system, with the two most prominent being electron-wave-function-based on the one hand and electron-density-based on the other hand.

1.3.1 *Ab initio* Methods: Hartree-Fock and Beyond

The family of *ab initio* methods generally tries to solve the (time independent) SCHRÖDINGER equation:[44]

$$\hat{H}|\psi\rangle = E|\psi\rangle \tag{1}$$

$\hat{H}$: HAMILTONIAN
$|\psi\rangle$: Vector notation of an n dimensional wave function
E : Energy eigenvalue of the wave function $|\psi\rangle$

For molecular systems, the HAMILTONIAN, the operator corresponding to the sum of all kinetic plus potential energies of all particles in a given system, generally takes the following form:

$$\hat{H} = \hat{T}_e + \hat{V}_{Ce} + \hat{V}_{ee} \tag{2}$$

$\hat{T}_e$: Operator of the kinetic energy of the electrons
$\hat{V}_{Ce}$: Operator of the potential energy of the core electron attraction
$\hat{V}_{ee}$: Operator of the potential energy of the electron electron repulsion

In quantum chemical systems, the nuclei are generally assumed to be stationary (BORN-OPPENHEIMER approximation).[45] Hence, the kinetic energy of the nuclei ($\hat{T}_C$) is neglected in the above description of the HAMILTONIAN. Also, the wave function is reduced to the description of the electronic configuration. Because of this, the family of *ab initio* methods can be considered as electron-wave-function-based approaches.

In principle, the solutions of the SCHRÖDINGER equation include the whole field of solid state physics and chemistry (neglecting relativistic effects). However, exact solutions exist only for one-electron systems like the hydrogen atom. For anything beyond, numerical techniques are required to approximate the interelectronic interactions.

Hartree-Fock Method The HARTREE-FOCK method[46]–[48] (HF) simplifies these interactions by describing the multi-electron wave function through a SLATER determinant. As a result,

[6] There is a certain similarity between this subchapter and a comparable subchapter in my Master's thesis.[1]

the individual electrons no longer interact in pairs, but with a field of all other particles in the so-called "mean field". The field still depends on the behaviour of the individual particles, but the solution can now be calculated gradually:

First, an initial state is selected from which the mean field is generated. Using this field, the SCHRÖDINGER equation is then solved for each individual particle. Together, the individual solutions then result in a new state and a new field. This process is repeated until successive solutions differ only slightly, resulting in a self-consistent field (SCF), i. e. the field leads to solutions that consistently generate the field itself again.

The systematic error, generated by neglecting the exact interaction of the electrons with each other, is called "electron correlation".

Post-Hartree-Fock Methods Building up on HF, various methods that are able to capture at least certain parts of the electron correlation have been developed. Of particular importance are the Configuration Interaction (CI)[49,50] and Coupled Cluster (CC)[51–53] methods as well as the MØLLER-PLESSET (MP) perturbation theory[54,55], which are all based on the solution of the HARTREE-FOCK method.

While inclusion of electron correlation generally drastically increases the accuracy of the calculations, one has to consider that especially for larger chemical systems, the computing time of these methods can easily exceed a human life time. Practically, quantum mechanical calculations of chemical systems are subjected to a compromise of accuracy and time, thus the choice of the calculational method is based on a constant trade-off between the best accuracy possible and a reasonable time scale to complete the calculation.

Arguably a "quantum step" forward was the recent development of the (linearly scaling) Domain-based Local Pair Natural Orbital Coupled Cluster (DLPNO-CC)[56] method. Including single, double and perturbed triple excitations, DLPNO-CCSD(T) recovers more than 99.9 % of the correlation energy of CCSD(T)[58] – which is often considered the gold-standard of computational chemistry[57] – while only taking twice to four times as long as a standard DFT calculation on the same system.[59]

Multi-Reference Methods A second important development from the HARTREE-FOCK method are multi-reference methods like the Complete Active Space Self-Constistent Field (CASSCF)[60–62] or the n-Electron Valence Perturbation Theory (NEVPT)[63–65] method. In contrast to the single-reference methods, these methods use linear combinations of multiple determinants in order to describe states that are not accurately calculated with a single determinant like e. g. (quasi-)degenerate ground states, low excitation states or bond breaking.

1.3.2 Density Functional Theory

Density Functional Theory (DFT) is a method to evaluate the energy of an N electron system without the complete solution of the SCHRÖDINGER equation by calculating the ground state

energy via the electron density ρ, which describes the system completely. One could say, instead of building up the wave function from scratch by trying to simulate the electrons one by one, one rather looks at the complete picture it draws. The advantage of this alternative compared to wave function based methods is the reduction of the necessary coordinates from $3N$ to 3.[7]

The (spin free) electron density can be considered as the probability of the presence of one of N electrons in the voxel $\mathrm{d}\vec{r}$ and is calculated by integrating the square of the N-electron wave function's absolute value over $N-1$ electron coordinates as well as N electron spins:

$$\rho(\vec{r}) = \rho(\vec{r}_1) = N \int \cdots \int |\psi(x_1, x_2, \ldots, x_N)|^2 \, \mathrm{d}s_1 \mathrm{d}x_2 \ldots \mathrm{d}x_N \tag{3}$$

The first HOHENBERG-KOHN theorem[66] states that the ground state energy $E_e[\rho]$ can be expressed as a functional of the ground state electron density ρ:

$$E_e[\rho] = \langle \psi | \hat{T}_e + \hat{V}_{Ce} + \hat{V}_{ee} | \psi \rangle = \mathcal{F}^{HK}[\rho] + E_{Ce}[\rho] \tag{4}$$

$\mathcal{F}^{HK}$: HOHENBERG-KOHN functional
E_{Ce} : Potential energy of the core electron attraction

Since $\hat{T}_e$ and $\hat{V}_{ee}$ only depend on the electron coordinates $\vec{r}$, their observables can be condensed to the functional $\mathcal{F}^{HK}$. $\mathcal{F}^{HK}$ then only depends on N which can easily be calculated by integrating $\rho(\vec{r})$ over the complete space:

$$\int \rho(\vec{r}) \, \mathrm{d}\vec{r} = N \tag{5}$$

$\hat{V}_{Ce}$ however depends further on the core coordinates $\vec{r}_A$ as well as core charges Z_A. The number of cores M as well as $\vec{r}_A$ can be extracted from the maxima of $\rho(\vec{r})$ and Z_A through derivation of $\rho(\vec{r})$ at the core coordinates. This makes $\hat{V}_{Ce}$ dependent on the exact form of $\rho(\vec{r})$.

The second HOHENBERG-KOHN theorem states that $E_e[\rho]$ is variational ($\tilde{E}_0 \geq E_0$) which means that the electron density ρ can be achieved by systematical minimation of $E_e[\rho]$ through variation with eq. 5 as secondary condition, at least in principle.

The major problem of this method is the fact that the HOHENBERG-KOHN functional $\mathcal{F}^{HK}$ is unknown and has to be approximated. This means, the accuracy of $E_e[\rho]$ is directly dependent on the accuracy of the approximation of $\mathcal{F}^{HK}$. To minimize the error, KOHN and SHAM divided the HOHENBERG-KOHN functional $\mathcal{F}^{HK}$ into the non correlating kinetic energy T_0^{KS}, the electron electron repulsion J^{KS} and the exchange/correlation functional E_{XC}.[67] The latter contains all unknown values and can be approximated by different methods:

Local Density Approximation (LDA). The basis of the LDA is the theory of the homogenous electron gas. E_{XC} is described as a function of the electron density ρ at the observed coordi-

[7] This is valid for the spin free electron density. Addition of the spin information leads to the addition of one further dimension.

nate. Through this approximation the exchange/correlation functional E_{XC} of a system with consistent electron density can be determined relatively accurately.

Generalized Gradient Approximation (GGA). Compared to the LDA, the GGA also considers the gradient of the electron density ρ, i.e. the derivative with respect to the position. This approach describes the inhomogenities of ρ in atoms and molecules better than LDA. The results of molecule geometries or ground state energies calculated with this method are generally relatively accurate.

Hybrid Approaches. If E_{XC} is calculated by a hybrid method, a part of the exchange energy is calculated via HF, the other part as well as the correlation energy via GGA and/or LDA. The calculated energies finally contribute differently weighted to E_{XC}.[68]

Though there are multiple methods of a great variety, there is currently no universal method for calculations on organic molecules.[69] However, for computational investigations – especially into organic and inorganic reactions – DFT has shown to give an adequate compromise between accuracy and speed and is thus the general method of choice.[70]–[73]

1.3.3 Basis Sets

While the choice of the applied method is a major factor contributing to the accuracy of a quantum chemical calculation, another factor – arguably as relevant as the method – that has to be considered is the choice of basis sets. The function of the basis set is to model atomic orbitals (AO) as well as molecular orbitals (MO) by linear combination of basic functions $|\varphi_i\rangle$ which build the basis set:

$$|\psi\rangle = \sum_{i}^{n} c_i |\varphi_i\rangle \tag{6}$$

Though SLATER-type orbitals (STO) generally describe the shape of AOs best, GAUSSIAN-type orbitals (GTO) are generally preferred due to their more efficient application.[74]

Effective Core Potentials (ECP). Since the effect of the chemical environment on the core electrons can often be neglected, effective core potentials (ECP) or pseudopotentials (PP) can be used for a simplified description of the innermost electrons. They approximate the complex description of core electrons, which – especially for heavier atoms – are subject to increasing relativistic effects, through an effective potential. Above a certain cutoff radius r_C, this simplification matches with the complete relativistic description of the core electrons, leading to accurate valence properties despite this approximation.[68]

All-Electron Basis Sets. However, due to the steady growth of computational resources as well as the improvement of available methods – and moreover, because calculation of properties like X-ray absorption or Mößbauer spectra rely on an accurate (relativistic) description of the innermost core electrons, all-electron basis sets for elements beyond Krypton are increasingly becoming both, accessible and common. For the present work, the "Segmented All-Electron Relativistically Contracted" (SARC) Basis Sets, a set of scalar relativistic all-electron basis sets from the Neese group, should quickly be introduced.[75] The SARC basis set family follows a design principle in which the GTOs with biggest exponents, representing the innermost shells, are contracted (we could say "frozen") into a single orbital function, which leads to a significant speedup without relevant loss of accuracy.[76]–[81]

2 Objective and Methodology

The research vacancy that is attempted to be addressed in this thesis is the *umpolung* reaction of fluoride. The overall goal is the synthesis of a bench-stable and at the same time reactive electrophilic fluorinating reagent like *N*-fluorobenzenesulfonimide (NFSI) or F-TEDA, starting from fluoride as fluorine source. Such reaction would e. g. revolutionize the synthetic accessibility of ^{18}F-Tracers in high specific activity for Positron Emmission Tomography (PET). The knowledge generated and collected in this thesis is supposed to help achieve this objective in due time.

As this work focusses on the theoretical, quantum chemical analysis of molecular systems and reactions, all of the work presented in here was performed using the ORCA program package.[82],[83] In the following paragraphs, I will introduce my standard setup:

DFT calculations were normally performed with the `PBE0` functional[84] and the `def2-TZVP` basis set[85] including GRIMME's `D3` dispersion correction with the BECKE-JOHNSON damping scheme.[86],[87] The Resolution of Identity Approximation (RI)[88]–[90] was used for the COULOMB integrals with the `def2/J` auxiliary basis set[91] and for the HF exchange terms with the Chain of Spheres Approximation (`COSX`).[92]

In general, geometries were either built from scratch using the molecular builder in the Avogadro[93] program or extracted from a crystal structure, and either way subsequently optimized by DFT. Local minima were confirmed through frequency analysis. Self-consistent field (SCF) and optimization convergence criteria were set tightly (ORCA keywords "`TightSCF`" and "`TightOpt`"). Sometimes the integration grid was enlarged (ORCA keyword "`Grid6`") and convergence problems were mostly solved through employing alternative algorithms like `KDIIS` or `SOSCF`. Orbital analyses included quasi-restricted orbitals (QRO)[94] and unrestricted corresponding orbitals (UCO)[95] that were called with the ORCA keywords "`UNO`" and "`UCO`".

CASSCF calculations generally started from DFT orbitals and geometries with the same basis sets, utilizing `TrafoStep RI` with the `def2/JK` auxilliary basis sets[96] and the AILFT module.[97],[98] SCF convergence criteria were also set tightly.

DLPNO-CCSD(T) calculations generally started from DFT geometries employing the `DKH2` scalar-relativistic HAMILTONIAN[99]–[105] and the relativistically recontracted `DKH-def2-TZVPP` basis sets.[85] For heavy elements ($Z > 36$), the `SARC-DKH-TZVPP` basis sets were used.[76] SCF convergence criteria were also set tightly, auxilliary basis sets were generated on the fly with the `AutoAux` command[106] and the Conductor-like Polarizable Continuum Model (`CPCM`)[107] was used to simulate implicit solvation in MeCN.

2.1 Representative Input File Headers

- A typical header for ground state geometry optimizations:

```
! PBE0 D3 Opt Freq RIJCOSX def2-TZVP def2/J TightSCF TightOpt
! (Grid6 NoFinalGrid / UNO / UCO / KDIIS / SOSCF)
```

- A typical header for a broken symmetry transition state optimization:

```
! PBE0 D3 OptTS Freq RIJCOSX def2-TZVP def2/J
! TightSCF TightOpt Grid6 NoFinalGrid
%scf brokensym 1,1 end
%geom calc_hess true end
```

- A typical header for a CASSCF calculation:

```
! MORead def2-TZVP def2/JK TightSCF
%casscf nel 3 norb 5 nroots 10 actorbs dorbs trafostep ri end
%MOInp "dft_opt.gbw"
```

- A typical header for a DLPNO-CCSD(T) calculation:

```
! DLPNO-CCSD(T) DKH-def2-TZVPP DKH2 AutoAux TightSCF
! CPCM(Acetonitrile)
%basis NewGTO Pt "SARC-DKH-TZVPP" end
NewAuxJGTO Pt "AutoAux" end
NewAuxJKGTO Pt "AutoAux" end
NewAuxCGTO Pt "AutoAux" end end
```

3 Results and Discussion

In this chapter I will present the most important research advances of my doctoral studies and try to set them into context.

3.1 "Palladium–catalysed electrophilic aromatic C–H fluorination"

When I started my doctoral studies in the RITTER group in 2016, we were in the middle of the development (incl. reaction analysis) of a palladium-catalyzed aryl C−H fluorination reaction.

Besides some laboratory work (incl. scanning of the substrate scope and mechanistic studies) I was mostly occupied with the computational analysis of the reaction mechanism. As it turned out, the fluorination of the arene, starting from the [Pd(IV)−F] complex, seems to proceed in a similar fashion as the former S_N2-type oxidative fluorination reaction: after an initial SET from the arene to the metal center, a fluoride anion is transferred, before a second electron is transferred. The corresponding transition state of this fluoride-coupled electron transfer reaction favors a broken spin symmetry solution. In Fig. 2, the resulting magnetic orbital pair is visualized as UCOs for the *para*-fluorination of chlorobenzene.

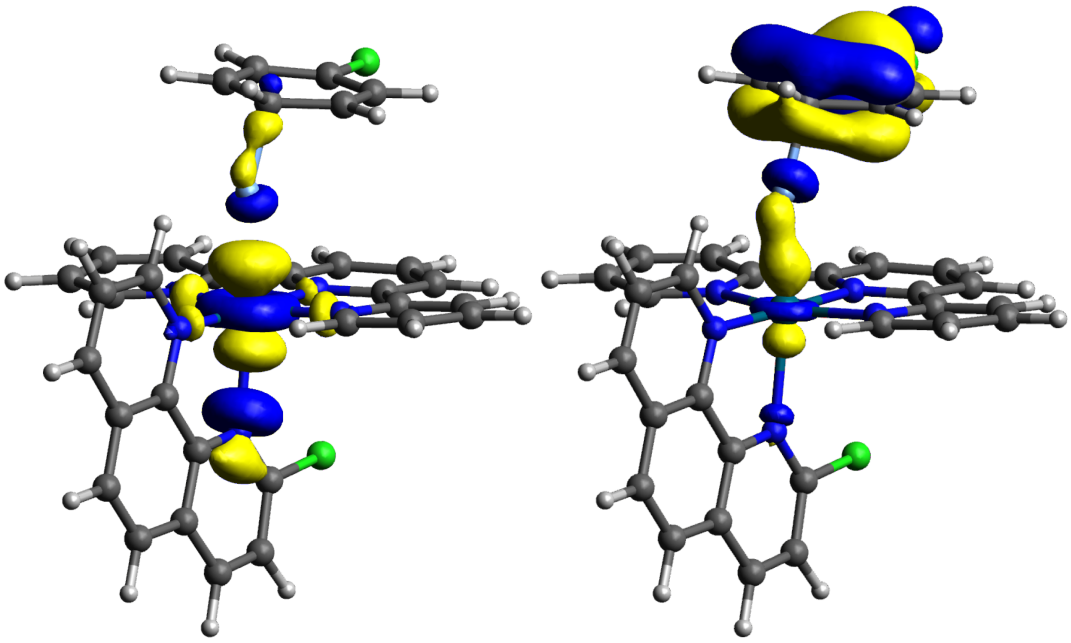

Figure 2: Visualization of the unrestricted corresponding orbitals (UCOs) representing the magnetic orbital pair of the palladium-catalyzed aryl C−H fluorination reaction's transition state: *para*-fluorination of chlorobenzene (left: alpha, right: beta; iso = 0.05).

This showed that the previously described SET/fluoride transfer/SET mechanism is a pattern generalizable to other systems as well – a second palladium fluoride complex that proceeds an oxidative fluorination through a fluoride coupled electron transfer reaction. It's a remarkably rare example for the single-electron reactivity of Pd (as Pd is known to highly prefer even oxidation states).[108]

The mechanistic analysis was included in the final publication of the reaction (A1.1).[2]

3.2 "Where Is the Fluoro Wall?: A Quantum Chemical Investigation"

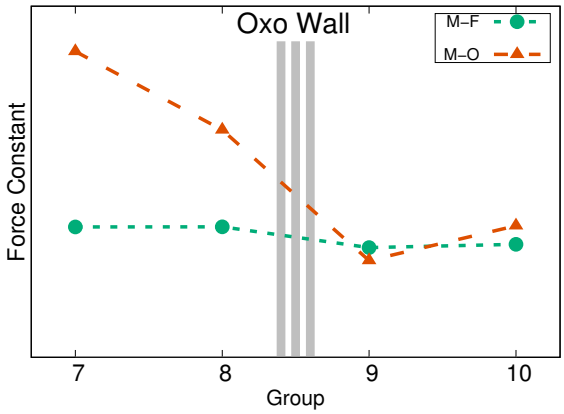

Figure 3: Graphical abstract of the publication "Where Is the Fluoro Wall?: A Quantum Chemical Investigation".[3]

After my transition to the NEESE group, my predominant research focus was to find an answer to the question: "Why is there a Nitrido and an Oxo Wall, but apparently no Fluoro Wall?" The long answer is appended (A1.2);[3] the short answer is: because the additional core charge pushes the $2p$ AO energies of the fluoro ligand too low to meaningfully π-interact with the empty metal d orbitals. For the oxo ligand, in contrast, the $2p$ AO's are energetically close enough to the metal d orbitals to form a proper π bond – or even two (cf. Fig. 4). This, however, comes with the price of extreme reactivity as soon as the d/π^* antibonding orbitals are filled with electrons; six-coordinate tetragonal oxo complexes beyond group 8 are stable *in silico* only.

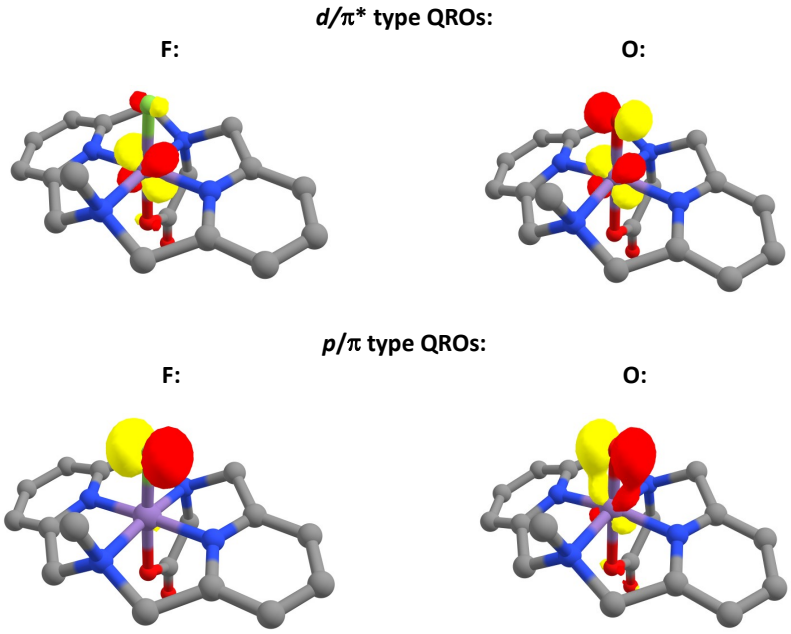

Figure 4: Representative d/π^* (top) and p/π (bottom) QROs for fluoro (left) and oxo (right) complexes (iso = 0.05).

3.3 "All-electron scalar relativistic basis sets for the elements Rb–Xe"

During my work on the computational analysis of several transition metal complexes, I came across the fact that in ORCA's `SARC` series of scalar-relativistic all-electron basis sets, no basis sets were provided for the 5th period elements, including the second-row transition metals (4*d* elements). So I developed them with the help of DIMITRIOS PANTAZIS. The corresponding publication is also appended (A1.3).[4]

We build a basis set in triple-ζ quality (`SARC-TZV`), consisting of 112 – 115 functions, contracted to 70 – 73 functions:

- (22s15p9d)[15s10p5d] for *s* and *d* block elements (Rb–Cd)
- (22s16p9d)[15s11p5d] for *p* block elements (In–Xe)

Additionally, we developed a polarization extension for DFT calculations (`P`), consisting of an additional *f* function for *d* and *p* block elements, and a correlation extension for post-HF methods (`PP`), consisting of an additional *f* function for *s* block elements, two additional *f* functions for *p* block elements, and one additional *d*, two *f*, and one *g* function(s) for *d* block elements.

3.4 The Train of Thought – Unfinished and Abandoned Ideas

The idea of this subchapter is to discuss those ideas that didn't succeed, but are still found worth being mentioned. The decision to include this chapter into this thesis follows two reasons: on the one hand I don't want this information to be wasted, maybe somebody else will find a fertile soil in these ideas. On the other hand, it's a political move. Our community is obsessed with success stories, with competition, with shining CV's. We rarely talk about things that didn't work, especially when it comes to official publications. I believe, every success story is only complete if it contains some information about the dead ends as well. So here are mine.

3.4.1 "Oxidative Activation of Fluoride for Organic Synthesis" – How It Started

The research objective addressed in Chapter 2 – the *umpolung* reaction of fluoride – started following me when I started my Master's thesis with TOBIAS RITTER.[1] The whole thesis deals with the synthesis of Pd(III) fluoride complexes that could potentially be able to fluorinate TEDA:

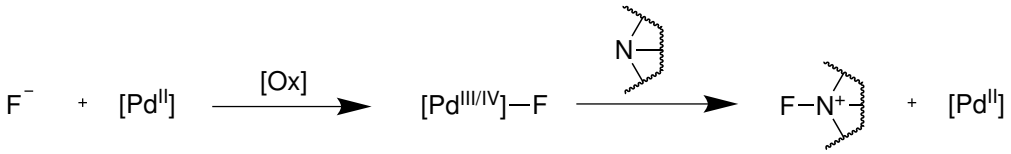

Scheme 2: General depiction of the desired *umpolung* reaction of fluoride.

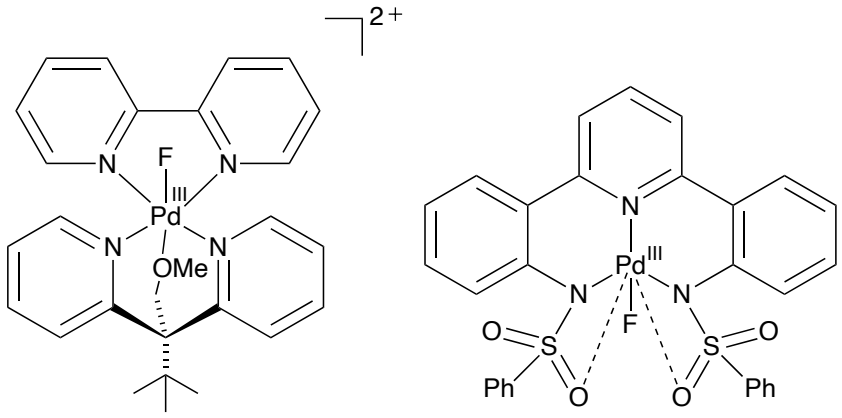

Scheme 3: Proposed complex structures for the reaction depicted in scheme 2.

Of course they didn't work. But that was not the end of the chase. During my doctoral studies, I followed this thought a couple more times into different directions. The overall objective, as given in scheme 2 stayed almost the same – the only change is that I started moving away from Pd as the metal center; I started looking e.g. into fluoride complexes of group 11 elements (Cu, Ag, Au), as well as Ru, Ir, Rh, Rh_2, and other bimetallic fluoride complexes that could electrophilically fluorinate TEDA.

3.4.2 Bismuth – The Next Big Player

At some point I stumbled upon Bismuth. It initially caught my attention due to a hint about the Bi–F bond being quite weak. I didn't find proper data to substantiate this claim, but I still started looking into the electronic structure of Bismuth. I started thinking about bimetallic systems with Pd and Bi, combining their properties, but discontinued that path quite early. Eventually, the reports from our institute by the CORNELLA group regarding Bi-catalyzed aryl fluorination[109] made me spark up that direction again.

The Bi(III)/(V) redox system has a beautiful and almost unique property – while the electronic system of Bi(V) has a completely empty valence shell, Bi(III) has a lone pair that can be localized in an sp^3-type orbital.

Scheme 4: Schematic structure of a possible Bi(III) complex with the electron pair in an sp^3-type orbital.

Based on this observation, I concluded that a Bi(V)–F complex could be a potent electrophilic fluorinating reagent; as a formal F^+ leaves the complex, the fluoride in the parent complex can just be replaced by the electron pair – electrophilic fluorination from a Bi(V) complex could potentially come without significant geometric change in the residual ligand sphere. The rest is ligand design.

So I came up with a couple of ligand framework structures and tried to modify the electronic properties in a way the Bi(V)–F would be able to fluorinate TEDA without decomposing itself. Unfortunately, I didn't find the sweet spot between reactivity and stability. Nevertheless, here are some structures I looked into:

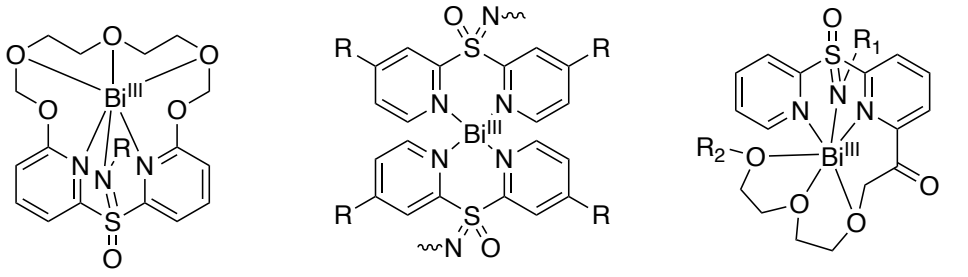

Scheme 5: Structural backbones of a row of investigated bismuth (III) complexes. The corresponding Bi(V)–F complexes were (unsuccessfully) analyzed regarding their potential to electrophilically fluorinate TEDA.

3.4.3 Back to Group Ten – Ni, Pd, Pt and the Spin Polarization Parameter

Actually, I never really left the group ten fluoride complexes. What eventually brought my focus back to the group 10 fluoride complexes were the reports of the RITTER group regarding an aryl C–F reductive elimination, starting from a M(II) complex with M = Ni, Pd.[110],[111] As it turned out, the reaction with Ni proceeds *via* a Ni(III)–F active intermediate,[112] while the reaction with Pd proceeds *via* a Pd(IV)–F active intermediate.[113] In order to understand where this difference comes from, the first thing I analyzed was the Potential Energy Surface (PES) (cf. Fig. 5) of the equilibrium given in scheme 6.

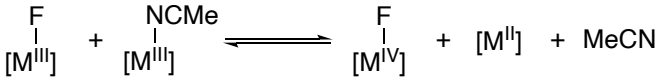

Scheme 6: Schematic equilibrium reaction of M(III)–F and M(IV)–F with M = Ni, Pd, Pt.

While the ΔG_{eq} values reported in fig. 5 are in beautiful agreement with the experimental observations by RITTER *et al.*,[110]–[113] the reason behind this observation is still not clear.

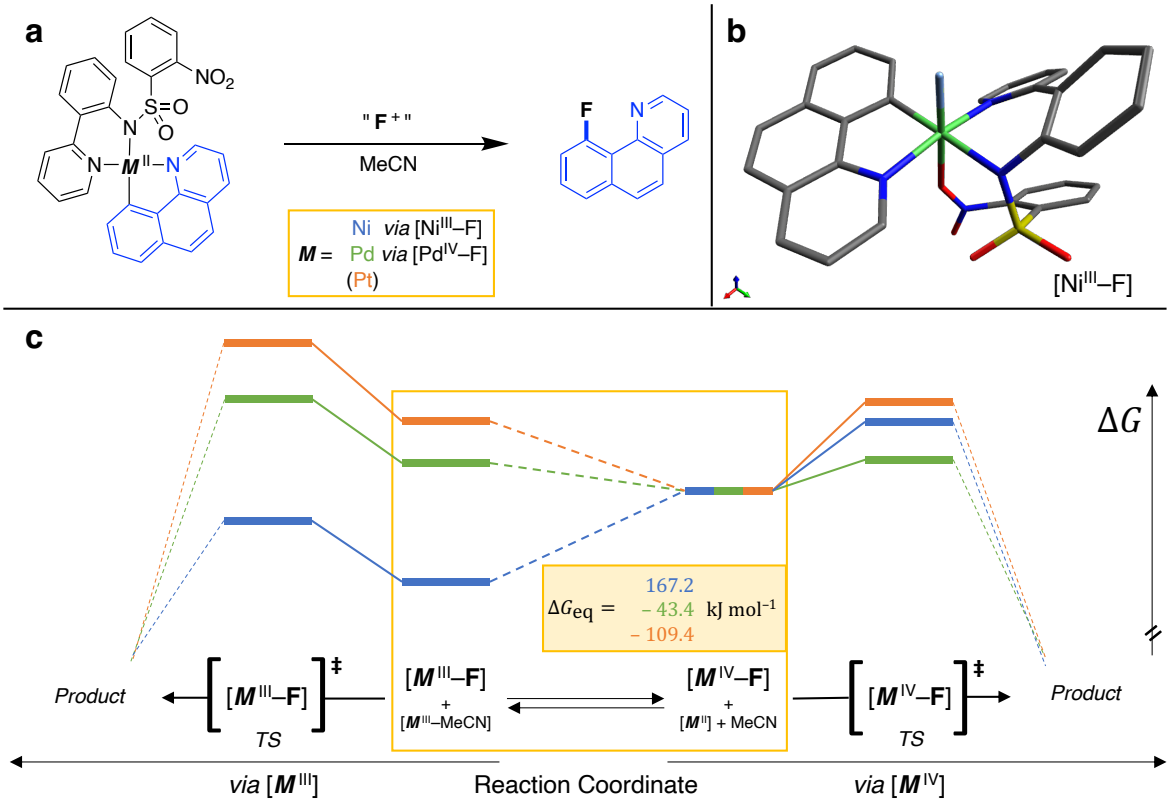

Figure 5: a: Lewis scheme of the investigated reaction by RITTER *et al.* **b**: Geometry of Ni(III)–F complex as a representative example. **c**: PES of the equilibrium, including the transition states of the following C–F bond forming reductive elimination reactions, as well as the calculated Free Energies for the displayed equilibrium reaction with M = Ni, Pd, Pt. Method: `(CPCM(MeCN) DLPNO-CCSD(T)/DKH2/SARC-DKH-TZVPP/DKH-def2-TZVPP//CPCM(MeCN) PBE0-D3/def2-TZVP)`.

Here is the current hypothesis: The individual spin orbitals of the doubly occupied orbitals in an open shell system tend to polarize ("split up" energetically). This splitting is highly dependent on the element. As it turns out, the spin orbitals in open shell systems of first row

transition metal systems tend to polarize stronger than those of second or third row transition metals. I am currently trying to parametrize this effect and show that the observed reactivity differences discussed above stem from the differences in these "Spin Polarization Parameters" (SPP).

Why should this spin polarization have such a clear effect on the energetics of the system? When the HOMO of a closed shell system loses one electron, the (now called) SOMO relaxes according to the spin polarizability of the system: the occupied α orbital goes down in energy, while the unoccupied β orbital goes up. As the α orbital is the only one occupied, the overall energy of the system goes down.

What now has to follow is the thorough parametrization of this spin polarizability, and the revelation of the (so far only hypothetical) connection between the resulting parameter and the observed reactivity trend. As this task turns out to be quite complex (and I'm already working on that for the better part of this year), this thesis is completed without the finalization of this project.

One thought, however, I will take out of this project: I have already previously learned that the F-TEDA radical cation is extremely unstable. Maybe the SET/fluoride transfer/SET reaction described above is not the right synthesis mode for F-TEDA, starting from fluoride. Hence, maybe exactly that observed single-electron reactivity of Ni and also Pd (even if less prominent) was the flaw of my approach so far. The proposed solution: move down in the periodic table. The next focus for the electrophilic fluorination of TEDA should maybe lie on Pt and Au – because they might transfer an F^+ without diverging any electron pairs and hence without generating the reactive F-TEDA radical cation intermediate.

4 Summary

The research advances discussed in this thesis include the mechanistic analysis of an aryl C–H fluorination reaction, the theoretical investigation into the electronic difference of oxo and fluoro ligands for transition metals and why there is an oxo (and nitrido) wall, but no fluoro wall, the generation of a segmented all-electron relativistically contracted basis set in triple-ζ quality, and the discussion of the advances on the way to the *umpolung* reaction of fluoride – which is how I call the synthesis of electrophilic fluorinating reagents like F-TEDA from fluoride – including the first introduction of the concept of a "Spin Polarization Parameter".

In summary, I am extremely happy this giant of a doctoral phase finally comes to an end. I hope the research advances described in this thesis help us as a scientific community to come closer to the objective of my research in the last half decade, said *umpolung* reaction of fluoride. Especially those thoughts described in the last subchapter are still full of potential – at least in my eyes. I will certainly not stop digging into these thoughts, as much as I hope they might also inspire others to do the same.

5 References

[1] J. D. Rolfes. *Oxidative Activation of Fluoride for Organic Synthesis*, F. Schoenebeck, T. Ritter; Max-Planck-Institut für Kohlenforschung, RWTH Aachen; **2016**.

[2] K. Yamamoto, J. Li, J. A. O. Garber, J. D. Rolfes, G. B. Boursalian, J. C. Borghs, C. Genicot, J. Jacq, M. van Gastel, F. Neese, T. Ritter. *Nature* **2018**, *554*, 511.

[3] J. D. Rolfes, M. van Gastel, F. Neese. *Inorg. Chem.* **2020**, *59*, 1556.

[4] J. D. Rolfes, F. Neese, D. A. Pantazis. *J. Comp. Chem.* **2020**, *41*, 1842.

[5] J. R. Winkler, H. B. Gray. In *Molecular Electronic Structures of Transition Metal Complexes I*; D. M. P. Mingos, P. Day, J. P. Dahl, Ed.; Springer Berlin Heidelberg: Berlin, Germany, **2011**; Vol. *142*, 17.

[6] B. Meunier, S. P. de Visser, S. Shaik. *Chem. Rev.* **2004**, *104*, 3947.

[7] H. B. Gray, J. R. Winkler. *Acc. Chem. Res.* **2018**, *51*, 1850.

[8] C. J. Ballhausen, H. B. Gray. *Inorg. Chem.* **1962**, *1*, 111.

[9] H. B. Gray, C. R. Hare. *Inorg. Chem.* **1962**, *1*, 363.

[10] G. Frenking, A. Krapp. *J. Comput. Chem.* **2007**, *28*, 15.

[11] K. K. Sunil, J. F. Harrison, M. T. Rogers. *J. Chem. Phys.* **1982**, *76*, 3087.

[12] C. D. Garner, J. Kendrick,P. Lambert, F. E. Mabbs, I. H. Hillier. *Inorg. Chem.* **1976**, *15*, 1287.

[13] N. Azuma, T. Ozawa, S. Tsuboyama. *J. Chem. Soc., Dalton Trans.* **1994**, *18*, 2609.

[14] R. S. Hay-Motherwell, G. Wilkinson, B. Hussain-Bates, M. B. Hursthouse. *Polyhedron* **1993**, *12*, 2009.

[15] E. Poverenov, I. Efremenko, A. I. Frenkel, Y. Ben-David, L. J. W. Shimon, G. Leitus, L. Konstantinovski, J. M. L. Martin, D. Milstein. *Nature* **2008**, *455*, 1093.

[16] D. Munz. *Chem. Sci.* **2018**, *9*, 1155.

[17] T. M. Anderson, W. A. Neiwert, M. L. Kirk, P. M. Piccoli, A. J. Schultz, T. F. Koetzle, D. G. Musaev, K. Morokuma, R. Cao, C. L. Hill. *Science* **2004**, *306*, 2074.

[18] K. P. O'Halloran, C. Zhao, N. S. Ando, A. J. Schultz, T. F. Koetzle, P. M. Piccoli, B. Hedman, K. O. Hodgson, E. Bobyr, M. L. Kirk, S. Knottenbelt, E. C. Depperman, B. Stein, T. M. Anderson, R. Cao, Y. V. Geletii, K. I. Hardcastle, D. G. Musaev, W. A. Neiwert, X. Fang, K. Morokuma, S. Wu, P. Kögerler, C. L. Hill. *Inorg. Chem.* **2012**, *51*, 7025.

[19] J. M. Winfield. *J. Fluorine Chem.* **1986**, *33*, 159.

[20] B. L. Pagenkopf, E. M. Carreira. *Chem. Eur. J.* **1999**, *5*, 3437.

[21] J. L. Kiplinger, T. G. Richmond, C. E. Osterberg. *Chem. Rev.* **1994**, *94*, 373.

[22] C. Hollingworth, V. Gouverneur. *Chem. Commun.* **2012**, *48*, 2929.

[23] N. Rozatian, I. W. Ashworth, G. Sandford, D. R. W. Hodgson. *Chem. Sci.* **2018**, *9*, 8692.

[24] D. O'Hagan, D. B. Harper. *J. Fluor. Chem.* **1999**, *100*, 127.

[25] T. Liang, C. N. Neumann, T. Ritter. *Angew. Chem. Int. Ed.* **2013**, *52*, 8214.

[26] P. Jeschke. *ChemBioChem* **2004**, *5*, 571.

[27] H.-J. Böhm, D. Banner, S. Bendels, M. Kansy, B. Kuhn, K. Müller, U. Obst-Sander, M. Stahl. *ChemBioChem* **2004**, *5*, 637.

[28] R. Berger, G. Resnati, P. Metrangolo, E. Weber, J. Hulliger. *Chem. Soc. Rev.* **2011**, *40*, 3496.

[29] F. Babudri, G. M. Farinola, F. Naso, R. Ragni. *Chem. Commun. (Camb.)* **2007**, 1003.

[30] K. Müller, C. Faeh, F. Diederich. *Science* **2007**, *317*, 1881.

[31] C. Isanbor, D. O'Hagan. *J. Fluor. Chem.* **2006**, *127*, 303.

[32] M. E. Phelps. *Proc. Natl. Acad. Sci. U.S.A.* **2000**, *97*, 9226.

[33] R. Bolton. *J. Labelled Compd. Radiopharm.* **2002**, *45*, 485.

[34] S. M. Ametamey, M. Honer, P. A. Schubiger. *Chem. Rev.* **2008**, *108*, 1501.

[35] L. Cai, S. Lu, V. W. Pike. *Eur. J. Org. Chem.* **2008**, 2853.

[36] P. W. Miller, N. J. Long, R. Vilar, A. D. Gee. *Angew. Chem. Int. Ed.* **2008**, *47*, 8998.

[37] R. Littich, P. J. H. Scott. *Angew. Chem. Int. Ed.* **2012**, *51*, 1106.

[38] J. F. Berry. *Comm. Inorg. Chem.* **2009**, *30*, 28.

[39] C. A. Laskowski, A. J. Miller, G. L. Hillhouse, T.R. Cundari. *J. Am. Chem. Soc.* **2011**, *133*, 771.

[40] T. Drews, J. Supel, A. Hagenbach, K. Seppelt. *Inorg. Chem.* **2006**, *45*, 3782.

[41] E. Lee, A. S. Kamlet, D. C. Powers, C. N. Neumann, G. B. Boursalian, T. Furuya, D. C. Choi, J. M. Hooker, T. Ritter. *Science* **2011**, *334*, 639.

[42] D. Seebach. *Angew. Chem. Int. Ed.* **1979**, *18*, 239.

[43] J. R. Brandt, E. Lee, G. B. Boursalian, T. Ritter. *Chem. Sci.* **2014**, *5*, 169.

[44] E. Schrödinger. *Phys. Rev.* **1926**, *28*, 1049.

[45] M. Born, R. Oppenheimer. *Ann. Phys.* **1927**, *389*, 457.

[46] (a) D. R. Hartree. *Proc. Camb. Phil. Soc.*, **1928** *24*, 89. (b) D. R. Hartree. *Proc. Camb. Phil. Soc.*, **1928** *24*, 111.

[47] V. Fock. *Z. Physik* **1930**, *62*, 795.

[48] D. R.Hartree, W. Hartree. *Proc. R. Soc. Lond. A.* **1935**, *150*, 9.

[49] B. Roos. *Chem. Phys. Lett.* **1972**, *15*, 153.

[50] J. A. Pople, R. Seeger, R. Krishnan. *Int. J. Quantum Chem.* **1977**, *12*, 149.

[51] F. Coester. *Nuc. Phys.* **1958**, *7*, 421.

[52] J. Čížek. *J. Chem. Phys.* **1966**, *45*, 4256.

[53] R. J. Bartlett, M. Musiał. *Rev. Mod. Phys.* **2007**, *79*, 291.

[54] C. Møller, M. S. Plesset. *Phys. Rev.* **1934**, *46*, 618.

[55] R. Krishnan, J. A. Pople. *Int. J. Quantum Chem.* **1978**, *14*, 91.

[56] C. Riplinger, F. Neese. *J. Chem. Phys.* **2013**, *138*, 034106.

[57] R. J. Bartlett. In *Theory and Applications of Computational Chemistry: The First Fifty Years*, C. E. Dykstra et al., Ed.; Elsevier: Amsterdam, Netherlands, **2005**.

[58] C. Riplinger, P. Pinski, U. Becker, E. F. Valeev, F. Neese. *J. Chem. Phys.* **2016**, *144*, 024109.

[59] D. G. Liakos, F. Neese. *J. Chem. Theory Comput.* **2015**, *11*, 4054.

[60] P. E. M. Siegbahn, A. Heiberg, B. O. Roos, B. Levy. *Phys. Scr.* **1980**, *21*, 323.

[61] B. O. Roos, P. R. Taylor, P. E. M. Siegbahn. *Chem. Phys.*, **1980**, *48*, 157.

[62] P. E. M. Siegbahn, J. Almlöf, A. Heiberg, B. O. Roos. *J. Chem. Phys.* **1981**, *74*, 2384.

[63] C. Angeli, R. Cimiraglia, S. Evangelisti, T. Leininger, J.-P. Malrieu. *J. Chem. Phys.* **2001**, *114*, 10252.

[64] C. Angeli, R. Cimiraglia, J.-P. Malrieu. *Chem. Phys. Lett.* **2001**, *350*, 297.

[65] C. Angeli, R. Cimiraglia, J.-P. Malrieu. *J. Chem. Phys.* **2002**, *117*, 9138.

[66] P. Hohenberg, W. Kohn. *Phys. Rev. B*, **1964**, *136*, 864.

[67] W. Kohn, L. J. Sham. *Phys. Rev. A*, **1965**, *140*, 1133.

[68] P. Atkins, R. Friedman. *Molecular Quantum Mechanics*, 4. Ed., Oxford U. P., Oxford, **2007**.

[69] R. Peverati, D. G. Truhlar. *Phil. Trans. R. Soc. A*, **2014**, *372*, 20120476.

[70] C. J. Cramer, D. G. Truhlar. *Phys. Chem. Chem. Phys.*, **2009**, *11*, 10757.

[71] L. Simon, J. M. Goodman. *Org. Biomol. Chem.*, **2011**, *9*, 689.

[72] Y. Minenkov, A. Singstad, G. Occhipinti, V. R. Jensen. *Dalton Trans.*, **2012**, *41*, 5526.

[73] A. J. Cohen, P. Mori-Sánchez, W. Yang. *Science*, **2008**, *312*, 792.

[74] J. G. Hill. *Int. J. Quantum Chem.* **2013**, *113*, 21.

[75] D. A. Pantazis, F. Neese. *WIREs Comput. Mol. Sci.* **2014**, *4*, 363.

[76] D. A. Pantazis, X. Y. Chen, C. R. Landis, F. Neese. *J. Chem. Theory Comput.* **2008**, *4*, 908.

[77] D. A. Pantazis, F. Neese. *J. Chem. Theory Comput.* **2009**, *5*, 2229.

[78] D. A. Pantazis, F. Neese. *J. Chem. Theory Comput.* **2011**, *7*, 677.

[79] D. A. Pantazis, F. Neese. *Theor. Chem. Acc.* **2012**, *131*, 1292.

[80] M. Dolg. *J. Chem. Theory Comput.* **2011**, *7*, 3131.

[81] D. Aravena, F. Neese, D. A. Pantazis. *J. Chem. Theory Comput.* **2016**, *12*, 1148.

[82] F. Neese. *WIREs Comput. Mol. Sci.* **2012**, *2*, 73.

[83] F. Neese. *WIREs Comput. Mol. Sci.* **2018**, *8*, e1327.

[84] C. Adamo, V. Barone. *J. Chem. Phys.* **1999**, *110*, 6158.

[85] F. Weigend, R. Ahlrichs. *Phys. Chem. Chem. Phys.* **2005**, *7*, 3297.

[86] S. Grimme, J. Antony, S. Ehrlich, H. Krieg. *J. Chem. Phys.* **2010**, *132*, 154104.

[87] S. Grimme, S. Ehrlich, L. Goerigk. *J. Comput. Chem.* **2011**, *32*, 1456.

[88] K. Eichkorn, O. Treutler, H. Öhm, M. Häser, R. Ahlrichs. *Chem. Phys. Lett.* **1995**, *240*, 283.

[89] K. Eichkorn, F. Weigend, O. Treutler, R. Ahlrichs. *Theor. Chem. Acc.* **1997**, *97*, 119.

[90] F. Neese. *J. Comput. Chem.* **2003**, *24*, 1740.

[91] F. Weigend. *Phys. Chem. Chem. Phys.* **2006**, *8*, 1057.

[92] F. Neese, F. Wennmohs, A. Hansen, U. Becker. *Chem. Phys.* **2009**, *356*, 98.

[93] M. D. Hanwell, D. E. Curtis, D. C. Lonie, T. Vandermeersch, E. Zurek, G. R. Hutchison. *J. Cheminf.* **2012**, *4*, 17.

[94] F. Neese. *J. Am. Chem. Soc.* **2006**, *128*, 10213.

[95] F. Neese. *J. Phys. Chem. Solids* **2004**, *65*, 781.

[96] F. Weigend. *J. Comput. Chem.* **2008**, *29*, 167.

[97] M. Atanasov, D. Ganyushin, K. Sivalingam, F. Neese. In *Molecular Electronic Structures of Transition Metal Complexes I*; D. M. P. Mingos, P. Day, J. P. Dahl, Ed.; Springer Berlin Heidelberg: Berlin, Germany, **2011**; Vol. *143*, 149.

[98] M. Atanasov, J. M. Zadrozny, J. R. Long, F. Neese. *Chem. Sci.* **2013**, *4*, 139.

[99] M. Douglas, N. M. Kroll. *Ann. Phys.* **1974**, *82*, 89.

[100] T. Nakajima, K. Hirao. *J. Chem. Phys.* **2000**, *113*, 7786.

[101] A. Wolf, M. Reiher, B. A. Hess. *J. Chem. Phys.* **2002**, *117*, 9215.

[102] C. van Wüllen. *J. Chem. Phys.* **2004**, *120*, 7307.

[103] M. Reiher, A. Wolf. *J. Chem. Phys.* **2004**, *121*, 10945.

[104] M. Reiher. *Theor. Chem. Acc.* **2006**, *116*, 241.

[105] M. Reiher. *WIREs Comput. Mol. Sci.* **2012**, *2*, 139.

[106] G. L. Stoychev, A. A. Auer, F. Neese. *J. Chem. Theory Comput.* **2017**, *13*, 554.

[107] M. Cossi, N. Rega, G. Scalmani, V. Barone. *J. Comput. Chem.* **2003**, *24*, 669.

[108] A. F. Holleman, E. Wiberg, N. Wiberg. *Lehrbuch der Anorganischen Chemie*, 101. Ed., Walter de Gruyter, Berlin, **1995**, 1589.

[109] O. Planas, F. Wang, M. Leutszch, J. Cornella. *Science*, **2020**, *367*, 313.

[110] E. Lee, J. M. Hooker, T. Ritter. *J. Am. Chem. Soc.* **2012**, *134*, 17456.

[111] T. Furuya, T. Ritter. *J. Am. Chem. Soc.* **2008**, *130*, 10060.

[112] H. Lee, J. Börgel, T. Ritter. *Angew. Chem. Int. Ed.* **2017**, *56*, 6966.

[113] T. Furuya, D. Benitez, E. Tkatchouk, A. E. Strom, P. Tang, W. A. Goddard III, T. Ritter. *J. Am. Chem. Soc.* **2010**, *132*, 3793.

Eidesstattliche Erklärung

Hiermit erkläre ich, Julian David Rolfes, an Eides Statt, dass ich die vorliegende Arbeit mit dem Titel

„About chemical Trends in Transition Metal Complexes“

selbstständig und ohne Benutzung anderer als der angegebenen Quellen und Hilfsmittel sowie fremder Hilfe angefertigt habe.

Alle Stellen, die wörtlich oder sinngemäß aus veröffentlichten oder nicht veröffentlichten Schriften entnommen wurden, sind als solche kenntlich gemacht. Die Arbeit hat in gleicher oder ähnlicher Form noch keiner Prüfungsbehörde vorgelegen.

Zu den dieser Arbeit zugrundeliegenden Publikationen habe ich folgende Beiträge geleistet:

- „Palladium–catalysed electrophilic aromatic C–H fluorination“[2]: Vollständige computerchemische Evaluation; Mitarbeit an mechanistischen Studien, Substrat-Scope, Datenanalyse.
- „Where Is the Fluoro Wall?: A Quantum Chemical Investigation“[3]: Vollständige computerchemische Evaluation sowie Verfassen des Manuskriptes.
- „All-Electron Scalar Relativistic Basis Sets for the Elements Rb–Xe“[4]: Vollständige Entwicklung des Basissatzes; Mitarbeit an der Evaluation der Qualität sowie Verfassen des Manuskriptes.

(Ort, Datum) (Unterschrift)

A Appendix

Appended are all academic – or rather: topic-related (peer-reviewed) and other (not necessarily peer-reviewed) publications I worked on during the time of my doctoral studies at the MAX-PLANCK-INSTITUT FÜR KOHLENFORSCHUNG from 2016 to 2020.

A1 – Academic Publications

A1.1 "Palladium–catalysed electrophilic aromatic C–H fluorination"[2]

A1.2 "Where Is the Fluoro Wall?: A Quantum Chemical Investigation"[3]

A1.3 "All-electron scalar relativistic basis sets for the elements Rb–Xe"[4]

A2 – Other Publications

EDITORIAL CHANGE:
This part is removed from this copy.

The full version can be requested:
`info@a-h.institute`

A1.1 “Palladium–catalysed electrophilic aromatic C–H fluorination”[2]

LETTER

doi:10.1038/nature25749

Palladium-catalysed electrophilic aromatic C–H fluorination

Kumiko Yamamoto[1,2]*, Jiakun Li[1]*, Jeffrey A. O. Garber[1,2], Julian D. Rolfes[1,2], Gregory B. Boursalian[1,2], Jannik C. Borghs[2], Christophe Genicot[3], Jérôme Jacq[3], Maurice van Gastel[1], Frank Neese[1] & Tobias Ritter[1,2]

Aryl fluorides are widely used in the pharmaceutical and agrochemical industries[1,2], and recent advances have enabled their synthesis through the conversion of various functional groups. However, there is a lack of general methods for direct aromatic carbon–hydrogen (C–H) fluorination[3]. Conventional methods require the use of either strong fluorinating reagents, which are often unselective and difficult to handle, such as elemental fluorine, or less reactive reagents that attack only the most activated arenes, which reduces the substrate scope. A method for the direct fluorination of aromatic C–H bonds could facilitate access to fluorinated derivatives of functional molecules that would otherwise be difficult to produce. For example, drug candidates with improved properties, such as increased metabolic stability or better blood–brain-barrier penetration, may become available. Here we describe an approach to catalysis and the resulting development of an undirected, palladium-catalysed method for aromatic C–H fluorination using mild electrophilic fluorinating reagents. The reaction involves a mode of catalysis that is unusual in aromatic C–H functionalization because no organometallic intermediate is formed; instead, a reactive transition-metal-fluoride electrophile is generated catalytically for the fluorination of arenes that do not otherwise react with mild fluorinating reagents. The scope and functional-group tolerance of this reaction could provide access to functional fluorinated molecules in pharmaceutical and agrochemical development that would otherwise not be readily accessible.

Conventional methods for aromatic fluorination require elemental fluorine or similarly reactive reagents, which are unselective and require specialized equipment to handle safely[4]. Bench-stable electrophilic fluorinating reagents—such as *N*-fluoropyridinium salts, *N*-fluorobenzenesulfonimide (NFSI) and Selectfluor—are easier to handle but less reactive, and require either very electron-rich arenes or multiple equivalents of the arene to accomplish direct C–H fluorination[5,6]. Catalysis of aromatic C–H fluorination reactions has been reported using coordination-assistance to promote fluorination proximal to Lewis-basic functional groups, but such approaches are limited in scope to those substrates containing the required directing groups[7–10]. Advances in aliphatic C–H fluorination have been made[11], but currently there is no method for direct aromatic C–H fluorination with broad scope.

In our investigation into the catalysis of aromatic C–H fluorination reactions, we sought an approach that was distinct from the common C–H activation sequence in which C–H metalation precedes functionalization; with few exceptions[12–14], the conventional approach[15] requires multiple equivalents of the arene substrate to promote C–H metalation in the absence of a coordinating directing group. Instead, we sought to design catalysts with ancillary ligands that would favour the oxidation of the complex before any interaction with the substrate, giving rise to a reactive, high-valent metal-fluoride intermediate that is electrophilic at fluorine and capable of oxidative fluorine transfer to arenes. We designed the Pd(II) complex **1**, ligated simultaneously by a tridentate (terpyridine, terpy) and a bidentate (2-chloro-1,10-phenanthroline, 2-Cl-phen) ligand, which would be oxidized by electrophilic fluorinating reagents to yield the desired Pd(IV)–F complex **2** (Fig. 1b). The oxidation of doubly cationic **1** is promoted by a destabilizing interaction between the lone pair of the apical donor atom and the filled d_{z^2} orbital on Pd(II), which is readily apparent in the highest occupied molecular orbital of **1** as calculated by density functional theory (DFT) (Fig. 1c). X-ray diffraction corroborates the apical interaction: the

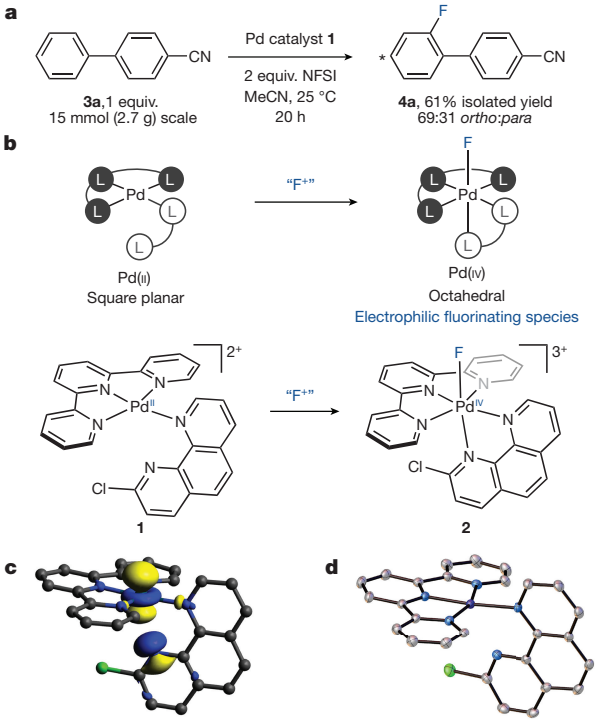

Figure 1 | Aromatic fluorination catalysed by 1. a, Palladium catalyst **1** enables the direct, non-chelation-assisted fluorination of 4-cyanobiphenyl. **b**, Oxidation of Pd(II) complex **1**, assisted by the ligand combination of terpy and 2-Cl-phen, yields the triply cationic Pd(IV)–F electrophile **2**. **c**, The highest occupied molecular orbital of **1**, as calculated by DFT, showing destabilizing orbital interaction. Hydrogen atoms are omitted for clarity. Calculations at the CPCM(MeCN)TPSS0 D3/def2-QZVP//PBE0 D3/def2-TZVP level of theory; iso = 0.05. **d**, X-ray crystal structure of **1**, shown with 50%-probability ellipsoids. Hydrogen atoms and solvent molecules are omitted for clarity.

[1]Max-Planck-Institut für Kohlenforschung, Kaiser-Wilhelm-Platz 1, D-45470 Mülheim an der Ruhr, Germany. [2]Department of Chemistry and Chemical Biology, Harvard University, 12 Oxford Street, Cambridge, Massachusetts 02138, USA. [3]Global Chemistry, UCB NewMedicines, UCB Biopharma, 1420 Braine-L'Alleud, Belgium.
*These authors contributed equally to this work.

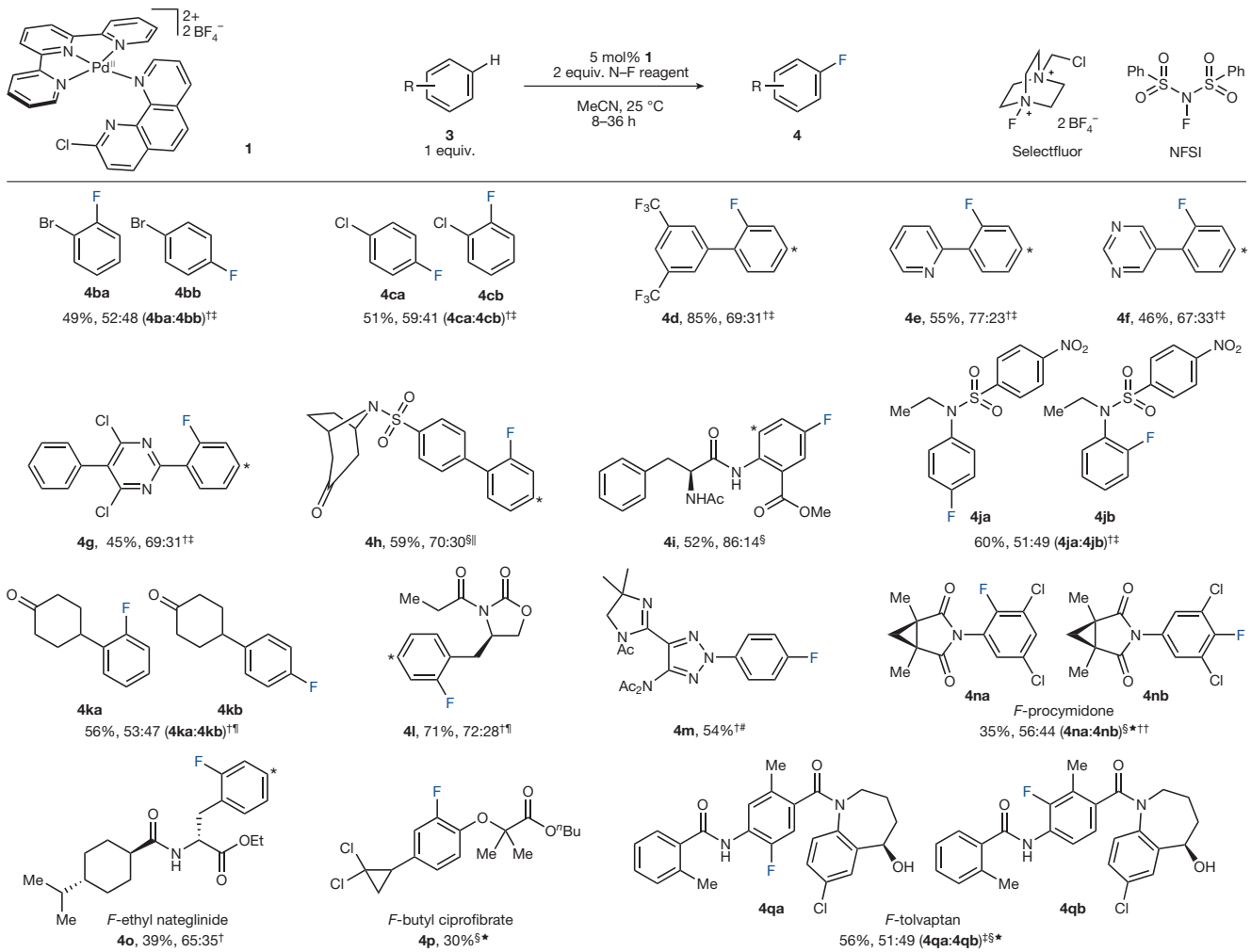

Figure 2 | Substrate scope of the Pd-catalysed fluorination of arenes. Reaction conditions: arene, 1 mmol; catalyst **1,** 5 mol%; Selectfluor or NFSI, 2 equiv.; MeCN, 0.1 M. All isomers of non-volatile products have been isolated and characterized as analytically pure samples. The asterisk denotes the site of fluorination of the constitutional isomer that is not shown. Overall yields and the ratio of the constitutional isomers are based on ^{19}F NMR integration of reaction mixtures with internal standard. †Reaction performed with Selectfluor. ‡Reaction performed at 50 °C. §Reaction performed with NFSI. ‖Reaction performed with 1,2-dichloroethane and MeCN (1:1, 0.1 M). ¶Reaction performed at 0 °C. #10 mol% catalyst **1** was used. ⋆7.5 mol% catalyst **1** was used. ††Reaction performed at 80 °C.

Pd–N distance in the X-ray structure of **1** (Fig. 1d) is 2.6 Å, which is 1.2 Å shorter than the sum of the van der Waals radii of Pd and N (ref. 16).

Complex **1** is a competent catalyst for the fluorination of various arenes by either Selectfluor or NFSI. The substrates shown in Fig. 2 underwent fluorination in the presence of **1** at room temperature or at 50 °C, but little background reactivity was observed in the absence of **1** under otherwise identical conditions (maximum <1% yield) or even under reflux in acetonitrile (maximum 21% yield). In our studies, catalyst **1** was formed *in situ* from [Pd(terpy)(MeCN)](BF$_4$)$_2$ and 2-Cl-phen, but it can also be generated by combining the commercially available palladium source [Pd(MeCN)$_4$](BF$_4$)$_2$ and the ligands before the addition of the reactants. Compatible functional groups include nitriles (**3a**), aryl bromides (**3b**), chlorides (**3c**, **3g, 3n, 3p, 3q**), certain heterocycles (**3e**–**3g**, **3m**), sulfonamides (**3h**, **3j**), ketones (**3h**, **3k**), amides (**3i**, **3l**–**3o, 3q**), esters (**3i**, **3o, 3p**), carbamates (**3l**), ethers (**3p**) and free hydroxy groups (**3q**). Five-membered heteroarenes containing nitrogen (**3m**) can be tolerated, but oxidatively labile functional groups such as amines and thiols cannot, owing to their general incompatibility with electrophilic fluorinating reagents. Electron-deficient arenes such as **3b**–**3d** are not successfully fluorinated through conventional methodologies, but are suitable substrates for fluorination via catalysis with **1**. However, more electron-deficient arenes, such as methyl benzoate, are insufficiently reactive and undergo little or no conversion.

Structurally complex substrates—such the pesticide procymidone (**3n**), the type-2 diabetes drug nateglinide (**3o**), the lipid-lowering agent ciprofibrate (**3p**) and the hyponatremia drug tolvaptan (**3q**)—were fluorinated directly via catalysis with **1**. Although fluorine can impart desirable properties on pharmaceuticals and agrochemicals, fluorinated analogues of structurally complex molecules can currently be difficult to access; conventional fluorination methods failed to provide the fluorinated products shown in Fig. 2.

In most cases, the fluorination reaction affords mixtures of at least two constitutional isomers, resulting from similar rates of fluorination at the positions *ortho* and *para* to the aromatic substituents. Purification of aryl fluoride products from mixtures of their constitutional isomers and the starting material is often challenging[17,18]. However, the isolation and characterization of all the non-volatile products obtained here has been achieved, although optimization of the separation protocol was required for each substrate. For example, the *ortho*- and *para*-fluorinated products of the gram-scale fluorination of 4-cyanobiphenyl have been separated in 61% isolated yield (Fig. 1a). Although high positional selectivity is generally desired in C–H functionalization reactions, mixtures of constitutional isomers can be advantageous for some applications. For example, in the late-stage derivatization of drug candidates, each product isomer is an additional derivative that can be obtained without the need for costly and laborious *de novo* synthesis[19,20]. Fluorinated tolvaptan

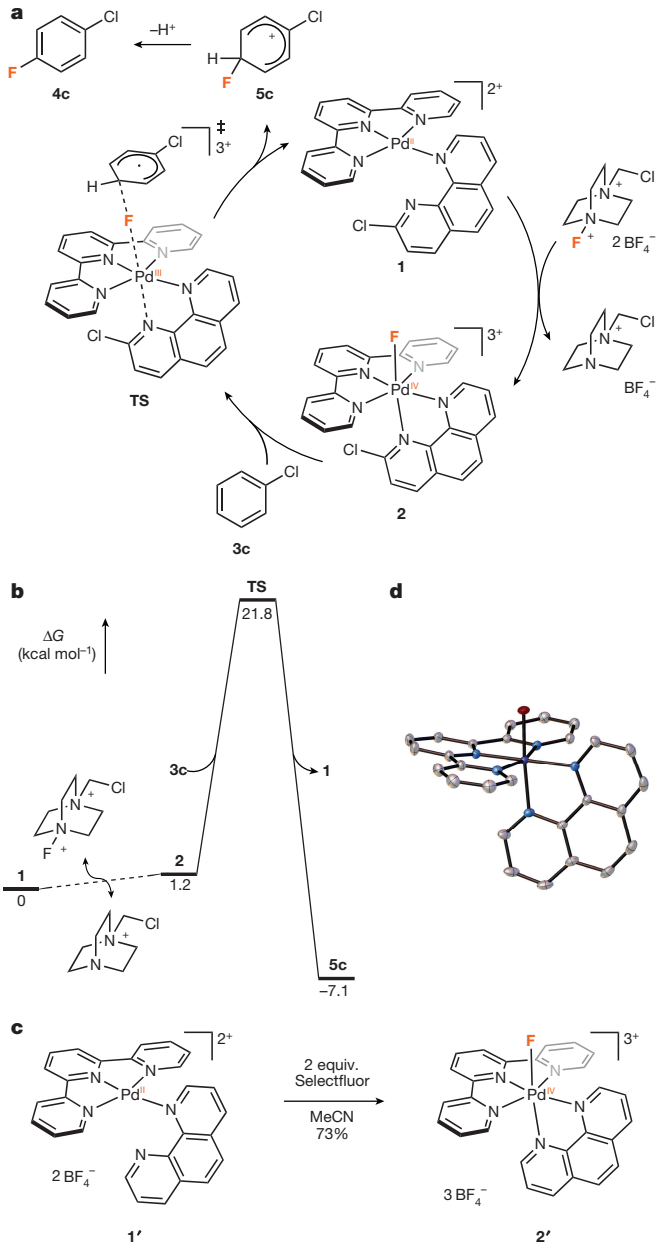

Figure 3 | Mechanism of fluorination catalysed by 1. a, The proposed catalytic cycle for the fluorination of chlorobenzene (**3c**). **b**, Energy-level diagram of the proposed catalytic cycle with chlorobenzene (**3c**); energies calculated by DFT. **c**, Synthesis of Pd(IV)–F complex **2′** via the oxidation of **1′** by Selectfluor. **d**, X-ray crystal structure of **2′**, shown with 50%-probability ellipsoids. Pd–F bond length: measured, 1.9120(7) Å; calculated, 1.89 Å.

(**4q**), for example, would be challenging and time-consuming to prepare with conventional chemistry through *de novo* syntheses. Late-stage fluorination, even with the requirement for a custom-made separation protocol, can conveniently produce promising new candidates that may have never been evaluated otherwise.

The proposed mode of action of **1** is highly unusual in the catalysis of aromatic oxidation reactions: conceptually, an activated electrophile is generated *in situ* from **1**, in the form of Pd(IV)–F intermediate **2**. The activated Pd(IV)–F electrophile **2** would therefore be capable of electrophilic fluorination of weakly nucleophilic arenes that cannot be fluorinated directly by Selectfluor and NFSI (Fig. 3a)[21,22]. A DFT analysis of the aryl fluorination reaction suggests a mechanism that is accessible to Pd(IV)–F **2** but not to Selectfluor or NFSI. On the basis of these results, we hypothesize that the fluorination mechanism proceeds through a single transition state via fluoride-coupled electron transfer (Fig. 3a, b).

Selectfluor fluorinates only electron-rich arenes such as anisole[23]; complex **1**, conversely, is able to catalyse the fluorination of electron-deficient arenes such as chlorobenzene. DFT calculations suggest that Pd(IV)–F **2** has a higher single-electron reduction potential than that of Selectfluor, although both compounds have a similar thermodynamic driving force for electrophilic fluorination. The transition state **TS** of the fluorination of chlorobenzene with Pd(IV)–F **2** shows high spin-density on the Pd as well as on the aryl carbon atoms. As such, the transition state is most appropriately characterized as a singlet diradical; two subsequent fluoride-coupled electron transfers occur asynchronously as the reaction proceeds through a single transition state. The mechanism is reminiscent of that previously reported for the fluorination of enamines and organometallic reagents with an isolated Pd(IV)–F (ref. 24). The calculated energy barrier for electrophilic fluorination of 21.8 kcal mol^{-1} (Fig. 3b) is in agreement with the observed reaction time and the temperature of the reaction (as discussed below, see Supplementary Information for details).

We sought to produce Pd(IV)–F complex **2**, to verify our design principle as well as to investigate the reactivity of **2** with arenes. Treatment of **1** with XeF_2 in the presence of $LiBF_4$ produced a ^{19}F NMR signal attributable to **2** at $\delta = -258.6$ p.p.m.; however, complex **2** is reduced to **1** in acetonitrile solution, even in the absence of substrate, which hindered our attempts at isolation. Treatment of **1** with Selectfluor over a range of temperatures (−40 °C to 25 °C) resulted in the desired reduction of Selectfluor, but did not produce a ^{19}F NMR signal that could be attributed to a Pd(IV)–F species, presumably because **2** is reduced faster than it is formed under these conditions, and therefore does not accumulate in observable quantities.

Complex **1′**, in which 2-Cl-phen is replaced with unsubstituted phenanthroline (phen), is a competent catalyst for aromatic fluorination, although not as effective as catalyst **1**. When **1′** was treated with Selectfluor in acetonitrile at room temperature and then allowed to stand at −35 °C, the Pd(IV)–F complex **2′** (^{19}F NMR −259.5 p.p.m.) precipitated in 73% yield (Fig. 3c). Complex **2′** is sufficiently stable at low temperature to enable characterization and reactivity studies. The higher stability of **2′** as compared to **2** is understood to result from the greater electron-donating ability of phen relative to that of 2-Cl-phen. Likewise, the greater reactivity of **2** may explain why the 2-Cl-phen-ligated complex **1** outperforms the phen-ligated **1′** in terms of catalytic ability.

Pd(IV)–F complex **2′** reacts with arenes to yield fluorinated products (Fig. 4). For example, 4-cyanobiphenyl (**3a**), when treated with **2′** in acetonitrile, yielded a 66:34 ratio of *ortho*- and *para*-fluoro isomers in 63% overall yield. The positional selectivity of fluorination by **2′** is similar to that observed in fluorination catalysed by **1′** (69:31 *ortho*:*para*), consistent with **2′** being the C–F-bond-forming species in catalysis by **1′**. These selectivity ratios are, in turn, similar to that observed upon fluorination with the optimal 2-Cl-phen-ligated catalyst **1** (71:29 *ortho*:*para*). We cannot rule out the involvement of a different C–F bond-forming pathway in catalysis by **1** (for example, through a Pd(III) species); however, the similar positional selectivities observed in fluorination catalysed by **1**, fluorination catalysed by **1′**, and stoichiometric fluorination by **2′** are consistent with fluorination by similar Pd(IV)–F species in all three cases, corresponding to **2** in the case of catalysis by **1**.

Aromatic C–H oxidations catalysed by transition metals generally proceed via C–H metalation followed by oxidation of the resulting organometallic intermediate, with product formation ensuing through reductive elimination. The aromatic fluorination catalysed by **1** presented here is an unusual example of an alternative mode of catalysis for aromatic C–H oxidation, in which a transition-metal catalyst is oxidized to a high-valent intermediate, which in turn oxidizes the substrate by group transfer of a ligand. Such an 'oxidation-first' mechanism is reminiscent of various transition-metal-catalysed aliphatic C–H oxidations, such as hydroxylations[25–27] and halogenations[28] through high-valent metal–oxo complexes, and aminations[29] via metal–nitrenoid

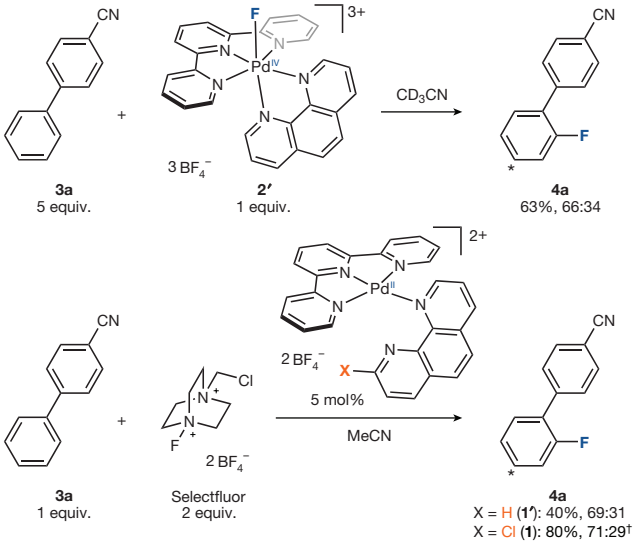

Figure 4 | Comparison of the positional selectivity of stoichiometric and catalytic fluorinations using 2′. Top, stoichiometric fluorination; bottom, catalytic fluorination. †5 equiv. of 4-cyanobiphenyl (**3a**) and 1 equiv. of Selectfluor were used.

species. Reported examples of such a mechanism for aromatic C–H oxidation, however, are rare, and are proposed to involve metal-nitrene or aminyl-radical transfer to the arene, although evidence for the proposed modes of action in these cases is indirect[30,31]. To the best of our knowledge, the aromatic fluorination reaction reported here is the only example so far of a synthetic method for aromatic C–H functionalization in which oxidation reactivity between a high-valent catalytic intermediate and arenes has been directly scrutinized.

The other examples of aromatic and aliphatic C–H oxidation reactions proceeding through 'oxidation-first' mechanisms mentioned above function because the high-valent intermediate provides access to a mechanism of oxidation that is not available to the starting reagents, such as a radical-rebound mechanism in the case of hydroxylation through metal–oxo intermediates. We have shown here data that support the interpretation that catalyst **2** provides access to a fluoride-coupled electron-transfer mechanism that is not accessible to electrophilic fluorinating reagents such as Selectfluor.

We anticipate that the direct electrophilic C–H fluorination of arenes reported here will be a useful tool in medicinal chemistry; indeed, the reaction has already found use in the late-stage derivatization of drug molecules. Furthermore, the unusual mechanism of catalysis by complex **1**, in which a high-valent transition-metal intermediate undergoes group transfer to arenes, may become the basis for a new approach to the catalysis of C–H functionalization reactions.

Data Availability Data are available from the corresponding author on reasonable request.

Received 21 March; accepted 17 December 2017.

1. Müller, K., Faeh, C. & Diederich, F. Fluorine in pharmaceuticals: looking beyond intuition. *Science* **317,** 1881–1886 (2007).
2. Gillis, E. P., Eastman, K. J., Hill, M. D., Donnelly, D. J. & Meanwell, N. A. Applications of fluorine in medicinal chemistry. *J. Med. Chem.* **58,** 8315–8359 (2015).
3. Campbell, M. G. & Ritter, T. Modern carbon–fluorine bond forming reactions for aryl fluoride synthesis. *Chem. Rev.* **115,** 612–633 (2015).
4. Sandford, G. Elemental fluorine in organic chemistry (1997–2006). *J. Fluor. Chem.* **128,** 90–104 (2007).
5. Taylor, S. D., Kotoris, C. C. & Hum, G. Recent advances in electrophilic fluorination. *Tetrahedron* **55,** 12431–12477 (1999).
6. Lal, G. S., Pez, G. P. & Syvret, R. G. Electrophilic NF fluorinating agents. *Chem. Rev.* **96,** 1737–1756 (1996).
7. Fier, P. S. & Hartwig, J. F. Selective C–H fluorination of pyridines and diazines inspired by a classic amination reaction. *Science* **342,** 956–960 (2013).
8. Chan, K. S. L., Wasa, M., Wang, X. & Yu, J.-Q. Palladium(II)-catalyzed selective monofluorination of benzoic acids using a practical auxiliary: a weak-coordination approach. *Angew. Chem. Int. Ed.* **50,** 9081–9084 (2011).
9. Wang, X., Mei, T.-S. & Yu, J.-Q. Versatile $Pd(OTf)_2{\cdot}2H_2O$-catalyzed *ortho*-fluorination using NMP as a promoter. *J. Am. Chem. Soc.* **131,** 7520–7521 (2009).
10. Hull, K. L., Anani, W. Q. & Sanford, M. S. Palladium-catalyzed fluorination of carbon–hydrogen bonds. *J. Am. Chem. Soc.* **128,** 7134–7135 (2006).
11. Liu, W. *et al.* Oxidative aliphatic C–H fluorination with fluoride ion catalyzed by a manganese porphyrin. *Science* **337,** 1322–1325 (2012).
12. Mkhalid, I. A. I., Barnard, J. H., Marder, T. B., Murphy, J. M. & Hartwig, J. F. C–H activation for the construction of C–B bonds. *Chem. Rev.* **110,** 890–931 (2010).
13. Cheng, C. & Hartwig, J. F. Rhodium-catalyzed intermolecular C–H silylation of arenes with high steric regiocontrol. *Science* **343,** 853–857 (2014).
14. Wang, P. *et al.* Ligand-accelerated non-directed C–H functionalization of arenes. *Nature* **551,** 489–493 (2017).
15. Kuhl, N., Hopkinson, M. N., Wencel-Delord, J. & Glorius, F. Beyond directing groups: transition-metal-catalyzed C–H activation of simple arenes. *Angew. Chem. Int. Ed.* **51,** 10236–10254 (2012).
16. Alvarez, S. A cartography of the van der Waals territories. *Dalton Trans.* **42,** 8617–8636 (2013).
17. Regalado, E. L., Makarov, A. A., McClain, R., Przybyciel, M. & Welch, C. J. Search for improved fluorinated stationary phases for separation of fluorine-containing pharmaceuticals from their desfluoro analogs. *J. Chromatogr. A* **1380,** 45–54 (2015).
18. Regalado, E. L. *et al.* Support of academic synthetic chemistry using separation technologies from the pharmaceutical industry. *Org. Biomol. Chem.* **12,** 2161–2166 (2014).
19. Hyohdoh, I. *et al.* Fluorine scanning by nonselective fluorination: enhancing Raf/MEK inhibition while keeping physicochemical properties. *ACS Med. Chem. Lett.* **4,** 1059–1063 (2013).
20. Cernak, T., Dykstra, K. D., Tyagarajan, S., Vachal, P. & Krska, S. W. The medicinal chemist's toolbox for late stage functionalization of drug-like molecules. *Chem. Soc. Rev.* **45,** 546–576 (2016); erratum **46,** 1760 (2017).
21. McCall, A. S. & Kraft, S. Pyridine-assisted chlorinations and oxidations by palladium(IV). *Organometallics* **31,** 3527–3538 (2012).
22. McCall, A. S., Wang, H., Desper, J. M. & Kraft, S. Bis-*N*-heterocyclic carbene palladium(IV) tetrachloride complexes: synthesis, reactivity, and mechanisms of direct chlorinations and oxidations of organic substrates. *J. Am. Chem. Soc.* **133,** 1832–1848 (2011).
23. Geng, C., Du, L., Liu, F., Zhu, R. & Liu, C. Theoretical study on the mechanism of selective fluorination of aromatic compounds with Selectfluor. *RSC Adv.* **5,** 33385–33391 (2015).
24. Brandt, J. R., Lee, E., Boursalian, G. B. & Ritter, T. Mechanism of electrophilic fluorination with Pd(IV): fluoride capture and subsequent oxidative fluoride transfer. *Chem. Sci.* **5,** 169–179 (2014).
25. Groves, J. T. High-valent iron in chemical and biological oxidations. *J. Inorg. Biochem.* **100,** 434–447 (2006).
26. McNeill, E. & Du Bois, J. Ruthenium-catalyzed hydroxylation of unactivated tertiary C–H bonds. *J. Am. Chem. Soc.* **132,** 10202–10204 (2010).
27. Chen, M. S. & White, M. C. A predictably selective aliphatic C–H oxidation reaction for complex molecule synthesis. *Science* **318,** 783–787 (2007).
28. Liu, W. & Groves, J. T. Manganese catalyzed C–H halogenation. *Acc. Chem. Res.* **48,** 1727–1735 (2015).
29. Du Bois, J. Rhodium-catalyzed C–H amination. An enabling method for chemical synthesis. *Org. Process Res. Dev.* **15,** 758–762 (2011).
30. Boursalian, G. B., Ngai, M.-Y., Hojczyk, K. N. & Ritter, T. Pd-catalyzed aryl C–H imidation with arene as the limiting reagent. *J. Am. Chem. Soc.* **135,** 13278–13281 (2013).
31. Paudyal, M. P. *et al.* Dirhodium-catalyzed C–H arene amination using hydroxylamines. *Science* **353,** 1144–1147 (2016).

Supplementary Information is available in the online version of the paper.

Acknowledgements We thank L. Gitlin for HPLC purification, R. Goddard, S. Palm and J. Rust for X-ray crystallographic analysis, C. Farès for NMR spectroscopy, and M. Blumenthal, D. Kampen and S. Marcus for mass spectrometry. We thank UCB Biopharma for funding and compound separation, the Japan Society for the Promotion of Science and L'Oréal-UNESCO Japan for graduate fellowships to K.Y., the Fonds der Chemischen Industrie for a graduate fellowship for J.D.R., and the German Academic Exchange Service, DAAD for an Otto-Bayer fellowship to J.C.B.

Author Contributions K.Y. designed catalyst **1** and optimized the fluorination reaction. K.Y. and J.D.R. conducted mechanistic studies. K.Y. and G.B.B. developed the conceptual approach to the project. J.L., J.A.O.G., J.C.B., K.Y. and J.D.R. explored the substrate scope. J.D.R. performed DFT calculations with input from M.v.G. and F.N. G.B.B. wrote the manuscript with input from all other authors. C.G. and J.J. supported development towards useful examples. K.Y., J.L., J.A.O.G., G.B.B., J.D.R. and T.R. analysed the data. T.R. directed the project.

Author Information Reprints and permissions information is available at www.nature.com/reprints. The authors declare no competing financial interests. Readers are welcome to comment on the online version of the paper. Publisher's note: Springer Nature remains neutral with regard to jurisdictional claims in published maps and institutional affiliations. Correspondence and requests for materials should be addressed to T.R. (ritter@kofo.mpg.de).

Reviewer Information *Nature* thanks J. Groves and the other anonymous reviewer(s) for their contribution to the peer review of this work.

A1.2 “Where Is the Fluoro Wall?: A Quantum Chemical Investigation”[3]

Inorganic Chemistry

Article

Cite This: *Inorg. Chem.* 2020, 59, 1556−1565

pubs.acs.org/IC

Where Is the Fluoro Wall?: A Quantum Chemical Investigation

Julian D. Rolfes, Maurice van Gastel,* and Frank Neese*

Max-Planck-Institut für Kohlenforschung, Kaiser-Wilhelm-Platz 1, D-45470 Mülheim an der Ruhr, Germany

Supporting Information

ABSTRACT: Despite their isoelectronic properties, fluoro and oxo ligands exhibit completely different chemical behavior. Formally speaking, the first is known to exclusively form single bonds, while the latter is generally observed to form double (or even triple) bonds. The biggest difference, however, lies in what is known among inorganic chemists as the Oxo Wall: the fact that six-coordinate tetragonal transition metal oxo complexes are not observed beyond group 7 elements. While the Oxo Wall was explained a few decades ago, some questions regarding the nature of the Oxo Wall remain unanswered. For example, why do group 8 oxo complexes with high oxidation states not violate the Oxo Wall? Moreover, why are transition metal fluoro complexes observed through the whole transition metal series? In order to understand how the small difference between these two isoelectronic ligands can give rise to such different chemical behaviors, we conducted an extensive computational analysis of the geometric and electronic properties of model fluoro and oxo complexes with metals around the Oxo Wall. Among many insights into the details of the Oxo Wall, we mostly learned that the oxygen 2p orbitals are prone to meaningfully interact with transition metal d orbitals, because they match not only spatially but also energetically, while for fluorine the p orbital energies are lower to an extent that interaction with transition metal d orbitals is much reduced. This in turn implies that in those instances where the metal d orbitals principally accessible for interaction are occupied, the oxygen 2p orbitals are too exposed to be stable.

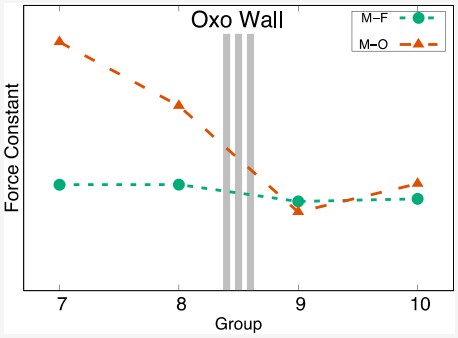

INTRODUCTION

The Oxo Wall is a widely known and accepted concept among the inorganic chemical community.[1] It states the instability of six-coordinate tetragonal oxo complexes with metals beyond group 8 (Figure 1).

7	8	9	10
25 Mn	26 Fe	27 Co	28 Ni
43 Tc	44 Ru	45 Rh	46 Pd
75 Re	76 Os	77 Ir	78 Pt

Figure 1. Depiction of the Oxo Wall surrounded by the investigated transition metals.

While transition metal oxo complexes are a prominent motif in biological oxidation processes,[2,3] the concept of the Oxo Wall dates back to 1962 when Ballhausen and Gray developed a molecular orbital energy level scheme that correctly described the electronic structure of the vanadyl ion.[4] The description of chromyl and molybdenyl ions followed shortly after, where the metal−oxo interaction was represented as a triple bond for the first time.[5] This notion is based on elementary molecular orbital considerations in which the bond order is deduced by subtracting the number of electrons in antibonding orbitals of a given bond from the number of electrons in the bonding counterparts of these orbitals and dividing the result by two.[6] For example, in the six-coordinate tetragonal oxo complex $Mo(V)OCl_5^{2-}$ the single d electron is found in the nonbonding d_{xy} orbital, leaving the two other d orbitals of t_{2g} symmetry (d_{xz} and d_{yz}) amenable to π interactions with the $p_{x/y}$ orbitals from the oxo ligand on the z axis (Figure 2). A total of six electrons are present in the two bonding π-orbitals and the bonding σ-orbital (interaction between oxo p_z and metal d_{z^2} orbital), while all antibonding counterparts are empty, thus leaving a metal−oxo triple bond.

The theoretical concept of the Oxo Wall—as stated by Gray and Winkler is as follows: "Complexes with tetragonal symmetry can have no more than 5 d electrons and still retain some MO multiple bonding. In the absence of π-bonding to the metal, the oxo will be extremely basic and unstable with respect to protonation or attack by electrophiles."[1] This is also supported by a large array of experimental investigations.[7−9] While oxo compounds are known with transition metals beyond the Oxo Wall[10,11] with well-characterized electronic structure,[12] these do not violate the concept of the Oxo Wall because they are not of tetragonal symmetry. Claims that exceptions have been found[13] were later retracted and as such, "the 'Oxo Wall' stands."[14]

Received: November 27, 2019
Published: January 7, 2020

DOI: 10.1021/acs.inorgchem.9b03474
Inorg. Chem. 2020, 59, 1556−1565

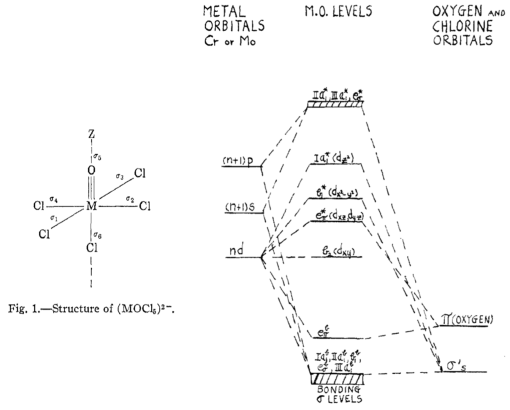

Fig. 1.—Structure of $(MOCl_5)^{2-}$.

Fig. 2.—Relative energies of the one-electron molecular orbitals for the $(MOCl_5)^{2-}$ molecule ion.

Figure 2. Original figures of Gray and Hare[5] that provided the historic foundation for the concept of the Oxo Wall. The figure depicts a metal oxo triple bond for the first time (left), reasoned by MO considerations (right). Reprinted from ref 5. Copyright 1962 American Chemical Society.

Extrapolation of this concept to the immediate neighbors of oxygen in the periodic table appear to be logical and seem to imply the existence of a Nitrido Wall as well as a Fluoro Wall. Interestingly, so far, nitrido complexes beyond the Nitrido Wall (which has the same location as the Oxo Wall) are not known, and even imido complexes are scarce.[15,16] In contrast, late transition metal fluoro complexes are widely observed and scrutinized.[17−19] Hence, the question arises, why do the considerations for the Oxo Wall not hold for the isoelectronic fluoro ligand? In order to answer this question, we investigate and compare the electronic properties of several *in silico* transition metal fluoro and oxo complexes around the Oxo Wall with the goal of understanding the differences between the fluoro and oxo ligands as well as to gain deeper insight into the electronic origin of the Oxo Wall.

In doing so, we took a strictly conceptual approach in which we studied *in silico* yet realistic models of transition metal oxo and fluoro complexes around the Oxo Wall (Figure 3). The

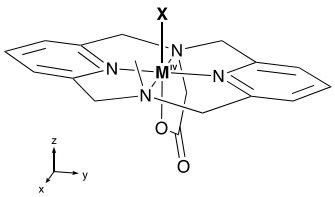

Figure 3. Schematic structure of the used model complex with indication of the coordinate system. The considered transition metals are given in Figure 1; X = F^- or O^{2-}.

study sheds light on the changes in the nature of the metal oxo and metal fluoro bonds, as well as in the electronic structure of the d manifold by employing density functional theory (DFT) as well as complete active space self-consistent field (CASSCF) followed by second-order N-electron valence perturbation theory (NEVPT2). We evaluate electronic properties, force constants, orbital splittings (*via ab initio* ligand field theory, AILFT),[20,21] and NMR shift parameters. Some of these properties are, in principle, amenable to experimental studies, while others serve illustrative and interpretative purposes.

METHODS

All computations were performed with the ORCA program package.[22,23] DFT calculations were performed with the PBE0 functional[24] and the def2-TZVP basis set[25] including Grimme's D3 dispersion correction with the Becke−Johnson damping scheme.[26,27] The resolution of identity approximation[28] was used for the Coulomb integrals with the def2/J auxiliary basis set[29] and for the Hartree−Fock exchange terms with the chain of spheres (COSX) approximation.[30] Unless otherwise noted, all geometries were built from scratch using the molecular builder in the Avogadro[31] program and subsequently optimized by DFT. Local minima were confirmed through frequency analysis. Self-consistent field (SCF) and optimization convergence criteria were set tightly (ORCA keywords "TightSCF" and "TightOpt"). These settings were used for the spin state and orbital analysis as well as the generation of all parameters given below except the AILFT and AOM parameters. Orbital analysis was carried out on the set of quasi-restricted orbitals (QRO)[32] (ORCA keyword "UNO").

For AILFT and AOM parameters, state-averaged complete active space self-consistent field (CASSCF)[33−35] calculations were performed on an active space of the five metal d-based orbitals (CAS(X,5)) with the def2-TZVP basis set and the AILFT module.[20,21] Tight SCF convergence criteria including the TrafoStep RI approximation with the def2-TZVP/JK auxiliary basis set were chosen,[36] starting from orbitals and geometries obtained by DFT calculations. The metal d-based orbitals were manually identified and rotated into the active space.

Molecules and orbitals were analyzed, and molecule pictures were created with Chemcraft.[37] Force constants were calculated with *orca_vib*, and orbital cube files were generated with *orca_plot*.[22,23]

Model Systems. One major limitation of the Oxo Wall concept is its applicability to six-coordinate tetragonal complexes only. In order to ensure an approximate six-coordinate tetragonal geometry for the calculated model complexes and to prevent undesired ligand dissociation, a highly tethered ligand system was chosen. The ligand system is based on aromatic and aliphatic amines in the *xy* plane of the metal center. These were chosen in order to minimize the interaction with the d orbitals of (approximate) t_{2g} symmetry, while retaining a rigid coordination geometry. Pyridyl ligands are known to act as π-acceptor ligands. However, for the highly oxidized systems of the present study, this effect should be negligible, and we have indeed not found any evidence for backbonding of the metal into the pyridyl ligand in the calculations. A carboxylate anchor was used trans to the X ligand (X = F or O). The negative charge of the carboxylate group ensures that it stays bound to the metal, even with a potentially strong trans effect that the ligand X may impose. A second important feature of the chosen ligand is its low propensity to form ligand radical complexes. This is important in order to properly focus on the electronic structure of the metal-X bond. While one could argue that there are practically no limitations regarding the complexity of the ligand, we have made an effort to keep the ligand as simple as possible. By choosing the N-substituted pyridinophane core structure, we ensure the applicability of our model system for future experimental investigations since several synthetic routes for this moiety have already been published.[38−40]

The considered oxidation state of the metal for all fluoro and oxo complexes of the 12 chosen transition metals surrounding the Oxo Wall is IV (cf. Figure 1). This oxidation state was chosen for two reasons: (1) For lower oxidation states the stability of the complexes is not guaranteed. (2) In oxidation state IV, the group 9 elements have 5 d electrons, which would theoretically be sufficient for the stabilization of an oxo ligand, which would conceptually be in violation of the Oxo Wall. However, group 9 oxo complexes with six-coordinate tetragonal geometry have not been observed experimentally, even in higher oxidation states. Therefore, using the oxidation state IV allows us to address this discrepancy between concept and experiment. As a final note, we state that the group 9 and 10 oxo complexes considered here do give stable complexes, albeit only under *in silico* and *in vacuo* conditions.

DOI: 10.1021/acs.inorgchem.9b03474
Inorg. Chem. 2020, 59, 1556−1565

RESULTS

Geometries. The M−X bond lengths of the most stable spin states (ground states) of the calculated complexes are summarized in Table 1. In addition, a N−M−N bond angle is given that refers to the pyridyl moieties on the *y*-axis. This angle is a reasonable measure for the deviation from six-coordinate tetragonal geometry, which is especially important for group 9 and 10 complexes (those beyond the Oxo Wall). The full spin-state analysis as well as the ground-state complex geometry coordinates are given in the Supporting Information.

Table 1. Group and Formal Metal d Electron Count, M−X Bond Lengths, (py)N−M−N(py) Bond Angles (along *y* Axis), and Ground-State Spin Multiplicities ($2S + 1$) for All Calculated M−X Complexes

		X = F			X = O		
group	metal center	M−F bond length [Å]	N−M−N angle [deg]	spin mult.	M−O bond length [Å]	N−M−N angle [deg]	spin mult.
7 (d^3)	Mn	1.769	176.1	4	1.655	166.5	4
	Tc	1.879	166.5	4	1.687	151.1	2
	Re	1.904	164.9	4	1.707	148.5	2
8 (d^4)	Fe	1.741	177.1	3	1.629	168.1	3
	Ru	1.848	167.5	3	1.753	162.1	3
	Os	1.874	166.0	3	1.782	159.7	3
9 (d^5)	Co	1.773	179.5	2	1.790	176.1	2
	Rh	1.905	176.7	2	1.892	171.6	2
	Ir	1.900	171.7	2	1.887	171.4	2
10 (d^6)	Ni	1.789	179.6	1	1.792	175.3	3
	Pd	1.923	179.3	1	1.899	177.8	1
	Pt	1.946	179.5	1	1.921	178.9	1

Force Constants. While bond lengths are known to be a reasonable indicator of bond strength, other geometric parameters like bond angles influence the M−X bond length and prevent a clear-cut correlation between the bond length and bond strength. Therefore, the M−X force constants were analyzed, because they provide a more direct and reliable measure of the bond strength (Figure 4). The force constants of the M−F bonds only show minor variations (2.7−4.2 mdyn/Å). The force constants of the M−O bonds, however, reveal a greater variance (1.9−7.9 mdyn/Å) with a clear and consistent discontinuity between group 8 and 9 elements, exactly at the location of the Oxo Wall.

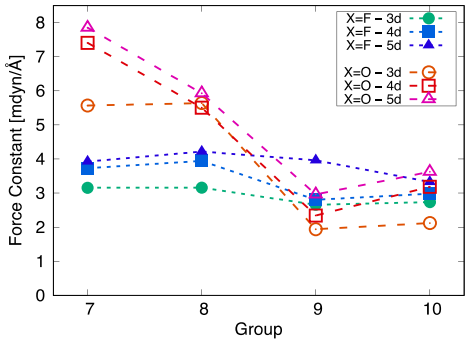

Figure 4. Force constants of M−X bonds for X = F and X = O. Exact values are given in the Supporting Information.

The force constants in Figure 4 indicate that the oxo ligand tends to form bonds of higher order for group 7 and 8 complexes whereas the fluoro ligand does not—which is in agreement with Lewis structure considerations and experimental observations,[41] and also with theoretical studies of transition metal fluoro complexes.[42,43] In order to understand the origin of this behavior, as well as the weak bonding of the oxo ligand with group 9 elements, the orbital structure of the complexes was analyzed.

Electronic Structure. *Orbital Pattern.* As a representative picture for all complexes, the 3d quasi-restricted orbitals (QRO) of the Mn−F and Mn−O complexes are presented in Figure 5.

As expected, the d-orbitals in the six-coordinate tetragonal complexes are separated into a low-lying t_{2g}-like set and a higher-lying e_g-like set, in accordance with approximate O_h symmetry. The lowest orbital is the nonbonding d_{xy} orbital. The large separation of the t_{2g} and e_g sets explains why most of the d^3 systems (Mn, Tc, Re) as exemplified in Figure 5 have a $S = 3/2$ ground state, why the d^4 systems (Fe, Ru, Os) are $S = 1$, why the d^5 systems (Co, Rh, Ir) are $S = 1/2$, and why most of the d^6 systems (Ni, Pd, Pt) are $S = 0$ (cf. Table 1). There are two exceptions to these general observations. The first is the low-spin configuration for the d^3 complexes Tc−O and Re−O ($S = 1/2$), which upon inspection of the orbital structure of these complexes is a consequence of the increased energy difference between the lowest nonbonding t_{2g} orbital and the two antibonding π^* type t_{2g} orbitals (intra-t_{2g} splitting). For Tc−O and Re−O, this energy gap is large enough that the double population of the lowest orbital is energetically favorable, leaving the highest t_{2g} orbital empty. The second is the Ni−O complex (d^6), which features a triplet ground state with a singly occupied orbital from the e_g set (*vide supra*). The localization and stabilization of the lowest e_g orbital indicates that the weakest ligand field is induced by the aliphatic nitrogen atoms of the ligand. We will come back to this subject later in the framework of the angular overlap model.

A thorough comparative analysis of the composition of the QROs of the fluoro and oxo complexes led to two interesting observations. Most noticeably, the oxo complexes of the group 9 elements as well as the Ni−O complex hold a singly occupied p orbital rather localized on the oxo ligand than on the metal (cf. Figure 6), even though this orbital formally constitutes the energetically highest orbital of the t_{2g} set. The presence of a singly occupied p(O) orbital implies a formal metal oxidation state of III instead of the expected oxidation state of IV, rendering the oxo ligand as an oxyl radical ligand. While one would intuitively expect the singly occupied orbital of the group 9 elements to be a metal d orbital, the large p(O) character of the e_g orbital indicates that the order of the d(M) and p(O) orbitals has changed and that from group 9 on, the p(O) orbitals are the highest (singly) occupied QROs. The formal oxidation state of III implies a d electron count of 6 instead of 5 for the group 9 elements, all located in the t_{2g} orbitals set. In other words, one could say that the p(O) orbitals can no longer sufficiently interact with the d(M) orbitals, resulting in a formal bond order of 1. Together with the reduced oxidation state of the metal and the transformation of the oxo ligand into a weaker bonding oxyl radical ligand, the significant and uniform reduction of the force constant for the group 9 M−O complexes (cf. Figure 4) is a logical consequence.

DOI: 10.1021/acs.inorgchem.9b03474
Inorg. Chem. 2020, 59, 1556−1565

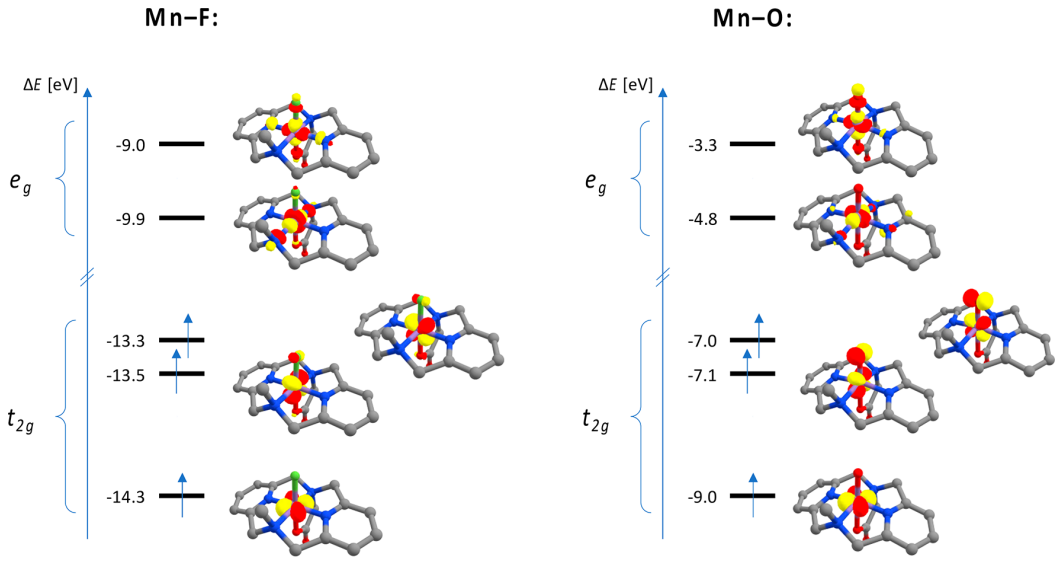

Figure 5. Representative orbital diagram for the d type QROs with energies, orbital pictures, and grouping terms ("t_{2g}", "e_g"; note that these are descriptive terms only and do not state actual degeneracy) of Mn–F (left) and Mn–O (right) complexes. Hydrogens are omitted for clarity (PBE0-D3/def2-TZVP, iso = 0.1).

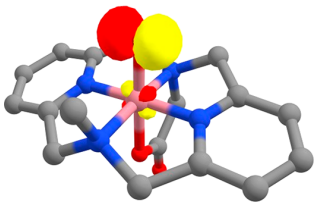

Figure 6. Singly occupied QRO of the Co–O complex. Hydrogens are omitted for clarity (PBE0-D3/def2-TZVP, iso = 0.1).

The latter analysis also holds true for the Ni–O complex, which is the only group 10 complex with a triplet ground state. The QROs reveal a singly occupied p(O) orbital as well as a singly occupied orbital that can be described as a d_{x^2}(Ni) orbital. These two orthogonal orbitals are close enough in energy to give rise to a high-spin configuration, resulting in a Ni(III) center with an oxyl radical ligand. Figure 7 gives a comprehensive overview of the electronic ground states of the calculated group 9 and 10 oxo and fluoro complexes. The increased d electron count in the Ni–O complex results in a bond length extension of all nickel–ligand bonds, most noticeably for the aliphatic amines, which are the weakest ligands. The force constant of the Ni–O bond, of a value in between those of the Co–O and the Rh–O bonds, is also in agreement with this interpretation (cf. Figure 4).

The elevated radical character on oxygen in the formal Co^{III}–O, Rh^{III}–O, and Ir^{III}–O complexes directly to the right side of the Oxo Wall (Figure 1) and that of the Ni^{III}–O complex explains why it has so far proven elusive to synthesize

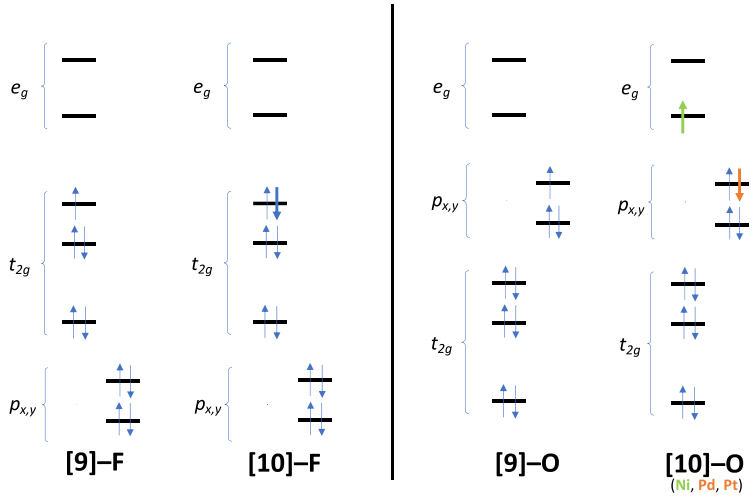

Figure 7. Qualitative depiction of the group 9 ([9]) and 10 ([10]) complexes' electronic ground states. The difference for the group 10 oxo complexes is shown through color: The green electron in the e_g orbital depicts the high-spin ground state of the Ni–O complex, while the orange electron in the p orbital depicts the low-spin ground state of the Pd–O and Pt–O complexes.

DOI: 10.1021/acs.inorgchem.9b03474
Inorg. Chem. 2020, 59, 1556–1565

such compounds. Even though the basic theoretical explanation of the Oxo Wall concept in principle allows for the existence of six-coordinate tetragonal group 9 oxo complexes with an oxidation state of IV and higher (and consequently the existence of tetragonal group 10 oxo complexes with an oxidation state of V and higher, and so on), the answer lies in the orbital order and the reactivity of the resulting oxyl species. Interestingly, throughout the analysis this behavior was never observed in any fluoro complex, which is consistent with the successful synthesis of six-coordinate tetragonal metal fluoro complexes with elements beyond group 8.[41]

The second observation also explains the tendency of the oxo ligand to form multiple bonds, while the fluoro ligand does not. Linear combination of a p(X) and d(M) atomic orbital results in a set of orbitals where the first can be denoted "p", after its major contributor, or "π", due to its bonding character, and the second can be denoted "d" or "π*". For the sake of the argument, the threshold for an atom-centered orbital denotation was set to 0.75. Orbital populations at X or M above this value were denoted p or d orbitals respectively, orbital populations below this value at X or M were denoted π- or π*-orbitals, dependent on their symmetry. It is clear that setting such a threshold to change nomenclature is somewhat arbitrary. However, no major conclusions are drawn that depend on the precise value of this threshold. Given that orbitals and populations are not physical observables, a discussion like the one we provide here is of a qualitative, chemical interpretation-oriented nature in the first place.

Choosing Mn as a specific example, Figure 8 compares the shape of one of the two sets of p/π- and d/π*-type QROs

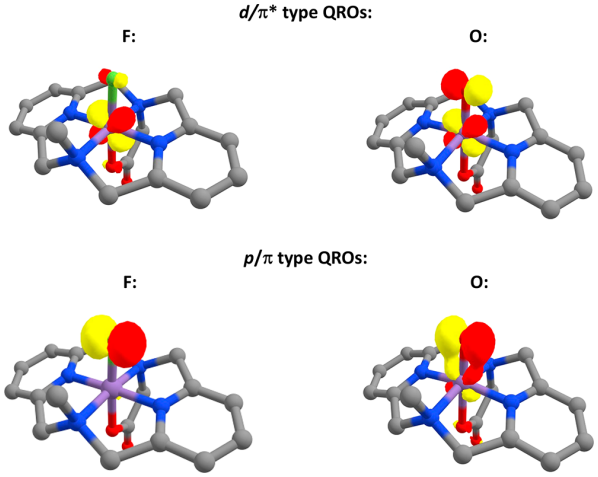

Figure 8. d_{yz}/π_y* and p_y/π_y QROs of Mn−X complexes for X = F (left) and X = O (right). Hydrogens are omitted for clarity (PBE0-D3/def2-TZVP, iso = 0.1).

between the Mn−F and Mn−O complexes. It becomes obvious that the AO-like p- and d-types of QROs dominate for the Mn−F complex, while the bonding/antibonding π- and π*-types of QROs dominate the Mn−O complex. This observation explains the tendency of the M−O complexes to form bonds of higher order, especially in those cases where the antibonding π*-type orbitals are not filled, while the M−F complexes do not have that propensity.

In order to quantify the p/π- and d/π*-type QRO shapes from Figure 8, Table 2 summarizes the mean Loewdin orbital

Table 2. Mean Loewdin Orbital Populations of p/π and d/π* QROs of Mn−X Complexes

Loewdin orb. population	X = F	p/π X = O	X = F	d/π* X = O
d(Mn)	0.07	0.23	0.85	0.65
p(X)	0.90	0.52	0.05	0.28

populations at Mn and X of the Mn−X complexes for X = F and X = O. On the basis of the specification above, the considered orbitals have been denoted p and d for X = F and π and π* for X = O. The enhanced π-bonding of the oxo ligand can be attributed to a higher covalency of the Mn−O bond compared to that of the Mn−F bond, which is also reflected in the Mn−X force constants (cf. Figure 4).

AILFT Analysis and AOM Parameters. In order to further quantify the ability of the oxo ligand over the fluoro ligand to form π-bonds with the coordinated metal, an AILFT analysis was performed. The AILFT module in ORCA deduces the d-orbital energies of a metal through the AILFT reconstruction of a CASSCF calculation that leads to a ligand field matrix $\mathbf{V}^{LFT}$ that is subsequently diagonalized to yield ligand field orbital energies.[20,21] From the 15 independent one-electron parameters of the AILFT Hamiltonian ($\mathbf{V}^{LFT}$), one can also extract ligand and metal specific M−L interaction parameters following the angular overlap model (AOM),[44−46] which can be interpreted as geometry-dependent splitting parameters for individual ligands. Details on the method used to calculate the AOM parameters as well as the full list of calculated parameters can be found in the Supporting Information.

Figure 9 shows a comparison of the d orbital splitting for the Mn−F and Mn−O complexes. While the individual values vary

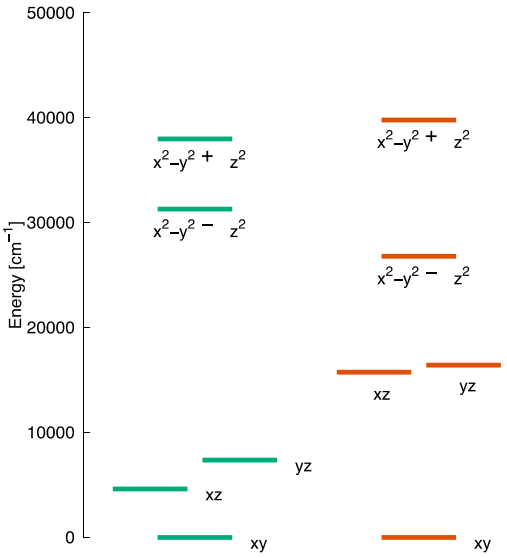

Figure 9. Splitting pattern (d orbital) for Mn−X model complex with X = F (left) and X = O (right).

through the series of evaluated metals, the qualitative picture from Figure 8 is consistent for the other metal complexes as well (for further details see the Supporting Information).

The most striking feature of Figure 9 is certainly the strongly reduced splitting in the t_{2g} set of orbitals for the fluoro ligand. Since the intra-t_{2g} splitting reflects π-bonding, this quantifies the statement that the fluoro ligand is far less involved in π-

DOI: 10.1021/acs.inorgchem.9b03474
Inorg. Chem. 2020, 59, 1556−1565

bonding than the oxo ligand. From the orbital splitting pattern in Figure 9, one can also see that the d_{xz} and d_{yz} orbitals are not completely degenerate. This is due to the influence of the carboxylate ligand, which imposes anisotropic π-donation. This anisotropic ligation results in an anisotropic trans effect on the X ligand, which while normally of isotropic nature, in turn also becomes anisotropic. Hence, the resulting AOM parameters are not only divided into e_σ and e_π, but the e_π parameter is again divided into $e_{\pi s}$ and $e_{\pi c}$. Because the subscripts "s" and "c" stand for "sine" and "cosine" and in spherical coordinate systems the azimuthal angle φ is defined to start at the x axis, $e_{\pi s}$ is defined as the parameter describing the influence of the X ligand on the d_{yz} orbital, and $e_{\pi c}$ is defined as the parameter describing the influence of the X ligand on the d_{xz} orbital. Hence, $e_{\pi s}$ is the parameter influenced more by the anisotropic trans effect of the carboxylate ligand, while $e_{\pi c}$ is expected to pose negligible influences.

Table 3 summarizes the three mean AOM parameters for the fluoro and oxo ligand as well as the individual differences

Table 3. Mean AOM Parameters with Standard Deviations (SD)

X	e_σ [cm^{-1}]	(SD)	$e_{\pi s}$ [cm^{-1}]	(SD)	$e_{\pi c}$ [cm^{-1}]	(SD)
F	15600	(3000)	2000	(1300)	3700	(1300)
O	20400	(6900)	10400	(2700)	13900	(1900)
diff.	4800		8400		10200	

between those two ligands. It is obvious from these values that the σ-donor propensity fluoride is only slightly lower than that of oxygen. However, the key difference is the oxo ligand's ability to form π-bonds, while the fluoride ligand is essentially non-π-bonding despite having occupied orbitals of the correct symmetry. This is reflected by the π-interaction parameters that are 4−5 times lower for the fluoro than for the oxo ligand (see also Figure 8).

Relative Orbital Energies. Because overlap (i.e., spatial interactions) between p(X) and d(M) orbitals is expected to be rather similar for X = F and O, the difference between F and O in the interaction between the p(X) and d(M) orbitals can presumably be attributed to their energy differences. In order to quantify the orbital energy differences, the following model was deployed. The QRO that most resembled a p(X) orbital was located, and the energy relative to the rather nonbonding d_{xy} QRO was determined and cached. The latter orbital energy, $\epsilon_{d_{xy}}$, is assumed to be independent from electronic interactions of the X ligand. For a given metal complex M, the relative energy difference between the p(F) and the p(O) orbital of the proper X ligand was subsequently estimated from the cached values:

$$\Delta E_M = (\Delta p_O - \Delta p_F)_M = (\epsilon_p - \epsilon_{d_{xy}})_{M-O} - (\epsilon_p - \epsilon_{d_{xy}})_{M-F} \quad (1)$$

The thus obtained p(X) orbital energy differences are plotted in Figure 10. The value of ΔE states in good approximation for each metal how much deeper the p(F) orbital lies relative to the p(O) orbital. Relative to the nonbonding d_{xy}(M) orbital, most of the p(F) orbitals are found between 2 and 3 eV lower than their p(O) counterparts, with the difference rising up to 3.6 eV. Furthermore, a clear slope can be identified to the right side of the location of the Oxo Wall. This slope can be

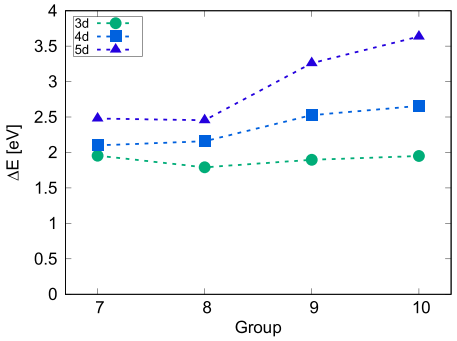

Figure 10. Energy difference of p(F) and p(O) according to eq 1.

attributed to the decreasing interaction between the p(O) and the d(M) orbitals going from group 7 to group 10 oxo complexes as already described above.

Natural Population Analysis and NMR Parameters. We address the final open question, the theoretical explanation of the instability of the closed shell group 10 oxo compounds (i.e. the Pd−O and the Pt−O complexes) through a natural population analysis (NPA), especially for the p(X) orbitals. Even without the significant radical character of the X ligands of the closed shell group 10 M−X complexes, the NPA reveals an electron deficiency especially on the oxo ligands, which after MO theory can be described as a singly bound ligand with a one-electron-equivalent formal charge remaining on the ligand. The NPA impressively shows that the p_z(O) orbitals for the Pd−O and Pt−O complexes, which are the orbitals mostly involved in the M−O σ-bond, lack nearly a full net electron. This makes the oxo ligand a strong electrophile and oxidant, likely resulting in complexes too reactive to be experimentally observed. Overall, the generally decreased population of the p_z(O) orbitals compared to the p_z(F) orbitals is also a strong argument for the rather covalent character of the M−O bond and the more ionic character of the M−F bond, in agreement with the afore-described findings of the orbital analysis. While the latter focused on the M−X π bonds, the NPA findings complement the analysis by addressing the covalency of the σ-bonds between the metals and the X ligands.

In order to correlate the results of the NPA to measurable quantities, NMR shifts of the closed shell complexes were calculated. Table 4 gives the calculated values of the NPA and

Table 4. Calculated NPA and NMR Parameters of Group 10 M−X Complexes

	Ni−X		Pd−X		Pt−X	
	X = F	X = O	X = F	X = O	X = F	X = O
NPA: Σp(X)[a]	5.640	4.601	5.654	5.019	5.653	5.106
NPA: p_z(X)	1.663	1.559[b]	1.672	1.085	1.670	1.196
NMR: δ(X) [ppm]	−288.7		−189.0	1251.9	−208.8	632.7

[a]Sum of NPA values of p_x(X), p_y(X), and p_z(X). [b]p_y(O) = 1.061.

of the NMR shifts. Comparing the overall p(X) population (row 1) with the NMR shifts, it becomes obvious that the lack of electron density on the X ligand correlates smoothly with the NMR shifts. This correlation can be explained through the deshielding effect on the nuclei by a less populated p(X) shell.

Comparison of the calculated NMR shifts in Table 4 with experimental data is difficult, because reported NMR shifts are

DOI: 10.1021/acs.inorgchem.9b03474
Inorg. Chem. 2020, 59, 1556−1565

found on an extremely wide range for both nuclei. ^{19}F NMR shifts of palladium fluoro complexes are typically found in the range of −274 to −323 ppm.[19,47−50] The example of a palladium difluoride with ^{19}F NMR shifts of −169 and −278 ppm, however, not only shows that the range of shifts is even greater but also shows that they can also drastically differ within the same complex.[51] For platinum fluoro complexes, the range of ^{19}F NMR shifts is even greater and typically spans from −107 to −456 ppm.[52,53] For nickel fluorides, ^{19}F NMR shifts are typically reported between −251 and −423 ppm.[54,55] In contrast to the fluoro complexes, the reported oxo complexes are purely hypothetical. Additionally, to the best of our knowledge, ^{17}O NMR shifts of group 10 oxo metal complexes are not reported. ^{17}O NMR shifts of other transition metal oxo complexes are reported between 775 and 1247 ppm.[56] For comparison, the proposed[13,57,58] and later retracted[14] late transition metal oxo complexes by Hill et al. had ^{17}O NMR shifts at 570, 590, and 605 ppm assigned to palladium and gold oxo complexes and a shift at 330 ppm assigned to a palladium hydroxo complex. All of them were later attributed to the polyoxotungstate ligands. While the calculated values for the fluoro complexes are in decent agreement with measured values of comparable complexes, the calculated values of the hypothetical oxo complexes are beyond the reported range, which is in agreement with the expected instability of the proposed structures.

DISCUSSION

In general,[59] the linear combination of two heteronuclear atomic orbitals A and B form a bonding/antibonding combination n/n^*, which can be approximately described as

$$n = N_1(\mathrm{A} + \alpha\cdot\mathrm{B}) \tag{2}$$

$$n^* = N_2(\mathrm{B} - \alpha\cdot\mathrm{A}) \tag{3}$$

with N_i being the normalization constants and α being an orbital weighing factor derived from first-order perturbation theory[60,61] and applied to extended Hückel theory:[62,63]

$$\alpha \propto \frac{\beta}{\epsilon_\mathrm{A} - \epsilon_\mathrm{B}} \tag{4}$$

with the resonance integral β and the atomic orbital energies ϵ_i. The Principle of Maximum Overlap[64−66] simplifies the correlation between the resonance integral β and the (spatial) overlap integral S_{AB} as

$$\beta \propto S_{AB} \tag{5}$$

The expected energy shift of the orbitals $\delta \approx \epsilon_n - \epsilon_\mathrm{A} \approx \epsilon_\mathrm{B} - \epsilon_{n^*}$ can be approximated as follows:

$$\delta \approx \frac{\beta^2}{\epsilon_\mathrm{A} - \epsilon_\mathrm{B}} \tag{6}$$

From eqs 2−5, it is obvious that there are two major factors influencing the mixing of orbitals A and B: the orbitals mix more for larger spatial overlap as well as for a smaller difference between the atomic orbital energies. This means that for $S_{AB} \to 0$ and for $\epsilon_\mathrm{A} \ll \epsilon_\mathrm{B}$ the values of n and n^* will resemble A and B, respectively (i.e., $\alpha = 0$), rather than a linear combination of A and B, also depicted by the vanishing energy shift of the orbitals as shown in eq 6. While this model is too simplistic to actually derive meaningful values from it, it paints a qualitative picture that is certainly sufficient to set the values calculated in the "Results" section into context.

In the first approximation (cf. eq 5), the resonance integral β can be treated as proportional to the spatial overlap of orbitals A and B. Due to the reduced charge of the fluoro ligand compared to the oxo ligand, the 1p orbitals of the fluoro ligand are expected to have a smaller radial expectation value than that of the oxo ligand and consequently also a reduced overlap. Indeed, the radial expectation values for the 1p orbitals were calculated as 1.21 and 1.58 Å for fluoride and oxide, respectively. The same trends that are obvious in Figure 4 can be expected to hold for β as well. This result is also consistent with the larger force constants calculated for the group 7 and 8 oxo complexes (cf. Table 1).

The calculated AOM parameters (cf. Table 3) can be interpreted as δ values (cf. eq 6) for different orbital interactions: $e_{\pi c}$ and $e_{\pi s}$ approximately equal δ for the interaction between the d_{xz}(M) and p_x(X), as well as d_{yz}(M) and p_y(X) orbitals, respectively. In addition, the ΔE values from Figure 10 (derived from eq 1) exactly quantify the difference between X = F and X = O as $\epsilon_{p(X)} - \epsilon_{d(M)}$. Hence, it can be directly deduced from these ΔE values that assuming a comparable β the δ values for X = F are expected to be smaller than those for X = O (because the denominator in eq 6 is bigger for X = F), which agrees with the AOM parameters.

Comparing eqs 4 and 6, one would expect a trend for α similar to that for δ. Indeed, comparing the mean Loewdin orbital populations from Table 2 (depicted in Figure 8), one can see that the orbital mixing between the p(X) and d(M) orbitals is much smaller for X = F than for X = O. This is the direct consequence of a smaller α value in eq 2, resulting from the larger orbital energy difference in eq 4 for X = F than for X = O.

The p(F) orbital has a lower energy than the p(O) orbital due to the higher effective nuclear charge experienced by the 2p electrons for fluorine since the increased nuclear charge of the fluorine nucleus is incompletely shielded by the other electrons. The difference of the p orbital energy between F and O has implications for the analyzed fluoro and oxo complexes: While the p(F) orbitals simply remain inaccessible for multiple bonding, the p(O) orbitals are so exposed that if not stabilized through d(M) interactions then a singly bound oxo ligand would be extremely reactive and hence unstable. In some instances met in our calculations, the oxidation potential of the metal center is already high enough to draw an electron out of a p(O) orbital, resulting in an oxyl radical complex. The NPA of the p_z(O) orbitals in Table 4 reveals that the oxo ligands in the hypothetical Pd−O and Pt−O complexes are so electron-deficient that they will likely react with even extremely weak electron donors by oxidation or oxygenation. Potential stabilization of those complexes by more electron-donating ligands to shift the electrons more toward the oxo ligand will instead result in increased basicity, eventually leading to already well-known and studied hydroxyl complexes (and probably deprotonated solvent).

Synthetically, we can think of two ways in which these results can be utilized. First, the energetic mingling of the d manifold and the p(O) orbitals observed for the group 9 and 10 oxo complexes leads to the formation of oxyl radical complexes in some cases. Tweaking the electronic properties of the ligand (e.g., by adding electron-withdrawing substituents like F, CF_3, or NO_2 to the pyridyl moieties) can potentially lead to an energetic stabilization of the d manifold, possibly

DOI: 10.1021/acs.inorgchem.9b03474
Inorg. Chem. 2020, 59, 1556−1565

strong enough to form oxyl radical complexes with group 8 or even group 7 metals. Further fine-tuning could eventually lead to "designer complexes" with oxyl character, potentially exhibiting unprecedented (catalytic) properties. Second, although chemically extremely challenging, we consider pushing the limits to a point where a late transition metal d manifold can be stabilized by extremely electron-withdrawing ligands to an extent where chemically meaningful interactions with the p(F) orbitals are possible, practically resulting in M−F multiple bonding. However, to date this has admittedly never been observed experimentally. The targeted search for such unusual compounds is, however, at the heart of chemical curiosity.

CONCLUSIONS

Through an extensive computational analysis of the geometric and electronic structure of a series of model complexes around the Oxo Wall, we solidified the theoretical foundation of the Oxo Wall concept. We have shown that the p orbitals of oxo ligands are energetically more readily accessible than the p orbitals of fluoro ligands by more than 2 eV. This leaves the fluoro ligand practically inaccessible for multiple bonding and the oxo ligand too reactive for formation of stable complexes with a singly bound oxo species. Hence, we conclude that there is no theoretically justifiable or practically meaningful concept of a Fluoro Wall. While the present analysis mostly focused on π-bonding, AOM and NPA analyses suggest that differences in σ-bonding also play a crucial role. According to our analysis, the M−F σ-bond seems to possess a rather ionic character, while the M−O σ-bond is of a more covalent nature, which is likely the source of the high electrophilicity and oxidative power of the oxo-complexes beyond the Oxo Wall, resulting in their practical instability. However, further research is required to evaluate the subtle differences in detail.

ASSOCIATED CONTENT

Supporting Information

The Supporting Information is available free of charge at https://pubs.acs.org/doi/10.1021/acs.inorgchem.9b03474.

Complete spin state analysis, Cartesian coordinates of all geometry optimized model structures, force constants, and full AILFT analysis, including AOM parameters- (PDF)

AUTHOR INFORMATION

Corresponding Authors

*E-mail: maurice.van-gastel@kofo.mpg.de (M.v.G.).
*E-mail: frank.neese@kofo.mpg.de (F.N.).

ORCID

Maurice van Gastel: 0000-0002-1547-6365
Frank Neese: 0000-0003-4691-0547

Notes

The authors declare no competing financial interest.

ACKNOWLEDGMENTS

Support by the Max Planck Society is gratefully acknowledged. J.D.R. thanks the Fonds der Chemischen Industrie for funding and Mihail Atanasov for insightful discussions regarding ligand-field theory.

REFERENCES

(1) Winkler, J. R.; Gray, H. B. In *Molecular Electronic Structures of Transition Metal Complexes I*; Mingos, D. M. P., Day, P., Dahl, J. P., Eds.; Springer Berlin Heidelberg: Berlin, Germany, 2011; Chapter 55, Vol. *142*, pp 17−28.
(2) Meunier, B.; de Visser, S. P.; Shaik, S. Mechanism of oxidation reactions catalyzed by cytochrome p450 enzymes. *Chem. Rev.* **2004**, *104* (9), 3947−80.
(3) Gray, H. B.; Winkler, J. R. Living with Oxygen. *Acc. Chem. Res.* **2018**, *51* (8), 1850−1857.
(4) Ballhausen, C. J.; Gray, H. B. The Electronic Structure of the Vanadyl Ion. *Inorg. Chem.* **1962**, *1* (1), 111−122.
(5) Gray, H. B.; Hare, C. R. The Electronic Structures and Spectra of Chromyl and Molybdenyl Ions. *Inorg. Chem.* **1962**, *1* (2), 363−368.
(6) Frenking, G.; Krapp, A. Unicorns in the world of chemical bonding models. *J. Comput. Chem.* **2007**, *28* (1), 15−24.
(7) Sunil, K. K.; Harrison, J. F.; Rogers, M. T. An SCF−MS−Xα study of a series of d1 transition metal oxohalo complexes. *J. Chem. Phys.* **1982**, *76* (6), 3087−3097.
(8) Garner, C. D.; Kendrick, J.; Lambert, P.; Mabbs, F. E.; Hillier, I. H. Single-crystal electronic spectrum of tetraphenylarsonium oxotetrachlorochromate(V), [C6H5)4As][CrOC14], and an ab initio calculation of the bonding and excited states of oxotetrachlorochromate(V). *Inorg. Chem.* **1976**, *15* (6), 1287−1291.
(9) Azuma, N.; Ozawa, T.; Tsuboyama, S. Spectroscopic studies of a square-pyramidal nitridochromium(V) complex. *J. Chem. Soc., Dalton Trans.* **1994**, No. 18, 2609.
(10) Hay-Motherwell, R. S.; Wilkinson, G.; Hussain-Bates, B.; Hursthouse, M. B. Synthesis and X-ray crystal structure of oxotrimesityliridium(V). *Polyhedron* **1993**, *12* (16), 2009−2012.
(11) Poverenov, E.; Efremenko, I.; Frenkel, A. I.; Ben-David, Y.; Shimon, L. J. W.; Leitus, G.; Konstantinovski, L.; Martin, J. M. L.; Milstein, D. Evidence for a terminal Pt(iv)-oxo complex exhibiting diverse reactivity. *Nature* **2008**, *455* (7216), 1093−1096.
(12) Munz, D. How to tame a palladium terminal oxo. *Chem. Sci.* **2018**, *9* (5), 1155−1167.
(13) Anderson, T. M.; Neiwert, W. A.; Kirk, M. L.; Piccoli, P. M.; Schultz, A. J.; Koetzle, T. F.; Musaev, D. G.; Morokuma, K.; Cao, R.; Hill, C. L. A late-transition metal oxo complex: K7Na9[O = PtIV(H2O)L2], L = [PW9O34]9. *Science* **2004**, *306* (5704), 2074−7.
(14) O'Halloran, K. P.; Zhao, C.; Ando, N. S.; Schultz, A. J.; Koetzle, T. F.; Piccoli, P. M.; Hedman, B.; Hodgson, K. O.; Bobyr, E.; Kirk, M. L.; Knottenbelt, S.; Depperman, E. C.; Stein, B.; Anderson, T. M.; Cao, R.; Geletii, Y. V.; Hardcastle, K. I.; Musaev, D. G.; Neiwert, W. A.; Fang, X.; Morokuma, K.; Wu, S.; Kogerler, P.; Hill, C. L. Revisiting the polyoxometalate-based late-transition-metal-oxo complexes: the "oxo wall" stands. *Inorg. Chem.* **2012**, *51* (13), 7025−31.
(15) Berry, J. F. Terminal Nitrido and Imido Complexes of the Late Transition Metals. *Comments Inorg. Chem.* **2009**, *30* (1−2), 28−66.
(16) Laskowski, C. A.; Miller, A. J.; Hillhouse, G. L.; Cundari, T. R. A two-coordinate nickel imido complex that effects C-H amination. *J. Am. Chem. Soc.* **2011**, *133* (4), 771−3.
(17) Drews, T.; Supel, J.; Hagenbach, A.; Seppelt, K. Solid state molecular structures of transition metal hexafluorides. *Inorg. Chem.* **2006**, *45* (9), 3782−8.
(18) Lee, E.; Kamlet, A. S.; Powers, D. C.; Neumann, C. N.; Boursalian, G. B.; Furuya, T.; Choi, D. C.; Hooker, J. M.; Ritter, T. A fluoride-derived electrophilic late-stage fluorination reagent for PET imaging. *Science* **2011**, *334* (6056), 639−42.
(19) Yamamoto, K.; Li, J.; Garber, J. A. O.; Rolfes, J. D.; Boursalian, G. B.; Borghs, J. C.; Genicot, C.; Jacq, J.; van Gastel, M.; Neese, F.; Ritter, T. Palladium-catalysed electrophilic aromatic C-H fluorination. *Nature* **2018**, *554* (7693), 511−514.
(20) Atanasov, M.; Ganyushin, D.; Sivalingam, K.; Neese, F. In *Molecular Electronic Structures of Transition Metal Complexes II*; Mingos, D. M. P., Day, P., Dahl, J. P., Eds.; Springer Berlin Heidelberg: Berlin, Germany, 2012; Vol. *143*, pp 149−220.
(21) Atanasov, M.; Zadrozny, J. M.; Long, J. R.; Neese, F. A theoretical analysis of chemical bonding, vibronic coupling, and

DOI: 10.1021/acs.inorgchem.9b03474
Inorg. Chem. 2020, 59, 1556−1565

magnetic anisotropy in linear iron(ii) complexes with single-molecule magnet behavior. *Chem. Sci.* **2013**, *4* (1), 139−156.
(22) Neese, F. The ORCA program system. *Wiley Interdisciplinary Reviews: Computational Molecular Science* **2012**, *2* (1), 73−78.
(23) Neese, F. Software update: the ORCA program system, version 4.0. *WIREs Comput. Mol. Sci.* **2018**, *8* (1), e1327.
(24) Adamo, C.; Barone, V. Toward reliable density functional methods without adjustable parameters: The PBE0 model. *J. Chem. Phys.* **1999**, *110* (13), 6158−6170.
(25) Weigend, F.; Ahlrichs, R. Balanced basis sets of split valence, triple zeta valence and quadruple zeta valence quality for H to Rn: Design and assessment of accuracy. *Phys. Chem. Chem. Phys.* **2005**, *7* (18), 3297−305.
(26) Grimme, S.; Antony, J.; Ehrlich, S.; Krieg, H. A consistent and accurate ab initio parametrization of density functional dispersion correction (DFT-D) for the 94 elements H-Pu. *J. Chem. Phys.* **2010**, *132* (15), 154104.
(27) Grimme, S.; Ehrlich, S.; Goerigk, L. Effect of the damping function in dispersion corrected density functional theory. *J. Comput. Chem.* **2011**, *32* (7), 1456−65.
(28) Neese, F. An improvement of the resolution of the identity approximation for the formation of the Coulomb matrix. *J. Comput. Chem.* **2003**, *24* (14), 1740−7.
(29) Weigend, F. Accurate Coulomb-fitting basis sets for H to Rn. *Phys. Chem. Chem. Phys.* **2006**, *8* (9), 1057−65.
(30) Neese, F.; Wennmohs, F.; Hansen, A.; Becker, U. Efficient, approximate and parallel Hartree−Fock and hybrid DFT calculations. A 'chain-of-spheres' algorithm for the Hartree−Fock exchange. *Chem. Phys.* **2009**, *356* (1−3), 98−109.
(31) Hanwell, M. D.; Curtis, D. E.; Lonie, D. C.; Vandermeersch, T.; Zurek, E.; Hutchison, G. R. Avogadro: an advanced semantic chemical editor, visualization, and analysis platform. *J. Cheminf.* **2012**, *4* (1), 17.
(32) Neese, F. Importance of direct spin-spin coupling and spin-flip excitations for the zero-field splittings of transition metal complexes: a case study. *J. Am. Chem. Soc.* **2006**, *128* (31), 10213−22.
(33) Roos, B. O.; Taylor, P. R.; Sigbahn, P. E. M. A complete active space SCF method (CASSCF) using a density matrix formulated super-CI approach. *Chem. Phys.* **1980**, *48* (2), 157−173.
(34) Siegbahn, P.; Heiberg, A.; Roos, B.; Levy, B. A Comparison of the Super-CI and the Newton-Raphson Scheme in the Complete Active Space SCF Method. *Phys. Scr.* **1980**, *21* (3−4), 323−327.
(35) Siegbahn, P. E. M.; Almlöf, J.; Heiberg, A.; Roos, B. O. The complete active space SCF (CASSCF) method in a Newton−Raphson formulation with application to the HNO molecule. *J. Chem. Phys.* **1981**, *74* (4), 2384−2396.
(36) Weigend, F. Hartree-Fock exchange fitting basis sets for H to Rn. *J. Comput. Chem.* **2008**, *29* (2), 167−75.
(37) *Chemcraft - Graphical Software for Visualization of Quantum Chemistry Computations*. https://www.chemcraftprog.com.
(38) Alpha, B.; Anklam, E.; Deschenaux, R.; Lehn, J.-M.; Pietraskiewiez, M. Synthesis and Characterisation of the Sodium and Lithium Cryptates of Macrobicyclic Ligands incorporating pyridine, bipyridine, and biisoquinoline units. *Helv. Chim. Acta* **1988**, *71* (5), 1042−1052.
(39) Bottino, F.; Di Grazia, M.; Finocchiaro, P.; Fronczek, F. R.; Mamo, A.; Pappalardo, S. Reaction of tosylamide monosodium salt with bis(halomethyl) compounds: an easy entry to symmetrical N-tosyl aza macrocycles. *J. Org. Chem.* **1988**, *53* (15), 3521−3529.
(40) Wessel, A. J.; Schultz, J. W.; Tang, F.; Duan, H.; Mirica, L. M. Improved synthesis of symmetrically & asymmetrically N-substituted pyridinophane derivatives. *Org. Biomol. Chem.* **2017**, *15* (46), 9923−9931.
(41) Winfield, J. M. Transition metal fluorides. *J. Fluorine Chem.* **1986**, *33* (1−4), 159−178.
(42) Abu-Hasanayn, F.; Goldman, A. S.; Krogh-Jespersen, K. Ab Initio Molecular Orbital Study of Substituent Effects in Vaska Type Complexes (trans-IrL2(CO)X): Electron Affinities, Ionization Potentials, Carbonyl Stretch Frequencies and the Thermodynamics of H2 Dissociative Addition. *Inorg. Chem.* **1994**, *33* (22), 5122−5130.
(43) Laitar, D. S.; Müller, P.; Gray, T. G.; Sadighi, J. P. A Carbene-Stabilized Gold(I) Fluoride: Synthesis and Theory. *Organometallics* **2005**, *24* (19), 4503−4505.
(44) Figgis, B. N.; Hitchman, M. A. *Ligand Field Theory and Its Applications*; John Wiley & Sons, Ltd.: New York, 2000.
(45) Jørgensen, C. K.; Pappalardo, R.; Schmidtke, H. H. Do the "Ligand Field" Parameters in Lanthanides Represent Weak Covalent Bonding? *J. Chem. Phys.* **1963**, *39* (6), 1422−1430.
(46) Schäffer, C. E.; Jørgensen, C. K. The angular overlap model, an attempt to revive the ligand field approaches. *Mol. Phys.* **1965**, *9* (5), 401−412.
(47) Fraser, S. L.; Antipin, M. Y.; Khroustalyov, V. N.; Grushin, V. V. Molecular Fluoro Palladium Complexes. *J. Am. Chem. Soc.* **1997**, *119* (20), 4769−4770.
(48) Marshall, W. J.; Thorn, D. L.; Grushin, V. V. Single-Crystal X-ray and Solution13C NMR Study of Fluoro(p-nitrophenyl)bis-(triphenylphosphine)palladium(II). Are There Effects of Through-Conjugation?†. *Organometallics* **1998**, *17* (24), 5427−5430.
(49) Jasim, N. A.; Perutz, R. N.; Whitwood, A. C.; Braun, T.; Izundu, J.; Neumann, B.; Rothfeld, S.; Stammler, H.-G. Contrasting Reactivity of Fluoropyridines at Palladium and Platinum: C−F Oxidative Addition at Palladium, P−C and C−F Activation at Platinum†. *Organometallics* **2004**, *23* (26), 6140−6149.
(50) Grushin, V. V.; Marshall, W. J. Facile Ar-CF3 bond formation at Pd. Strikingly different outcomes of reductive elimination from [(Ph3P)2Pd(CF3)Ph] and [(Xantphos)Pd(CF3)Ph]. *J. Am. Chem. Soc.* **2006**, *128* (39), 12644−5.
(51) Furuya, T.; Ritter, T. Carbon-fluorine reductive elimination from a high-valent palladium fluoride. *J. Am. Chem. Soc.* **2008**, *130* (31), 10060−1.
(52) Nilsson, P.; Plamper, F.; Wendt, O. F. Synthesis, Structure, and Reactivity of Arylfluoro Platinum(II) Complexes. *Organometallics* **2003**, *22* (25), 5235−5242.
(53) Yahav, A.; Goldberg, I.; Vigalok, A. Difluoro complexes of platinum(II) and -(IV) with monodentate phosphine ligands: an exceptional stability of d6 octahedral organometallic fluorides. *Inorg. Chem.* **2005**, *44* (5), 1547−53.
(54) Matwiyoff, N. A.; Asprey, L. B.; Wageman, W. E.; Reisfeld, M. J.; Fukushima, E. Fluorine-19 nuclear magnetic resonance studies of diamagnetic fluoride complexes of nickel(IV), palladium(IV), and platinum(IV) in anhydrous hydrogen fluoride solutions. *Inorg. Chem.* **1969**, *8* (4), 750−753.
(55) Meucci, E. A.; Ariafard, A.; Canty, A. J.; Kampf, J. W.; Sanford, M. S. Aryl−Fluoride Bond-Forming Reductive Elimination from Nickel(IV) Centers. *J. Am. Chem. Soc.* **2019**, *141* (33), 13261−13267.
(56) Fujii, H.; Kurahashi, T.; Tosha, T.; Yoshimura, T.; Kitagawa, T. 17O NMR study of oxo metalloporphyrin complexes: correlation with electronic structure of M = O moiety. *J. Inorg. Biochem.* **2006**, *100* (4), 533−41.
(57) Anderson, T. M.; Cao, R.; Slonkina, E.; Hedman, B.; Hodgson, K. O.; Hardcastle, K. I.; Neiwert, W. A.; Wu, S.; Kirk, M. L.; Knottenbelt, S.; Depperman, E. C.; Keita, B.; Nadjo, L.; Musaev, D. G.; Morokuma, K.; Hill, C. L. A Palladium-Oxo Complex. Stabilization of This Proposed Catalytic Intermediate by an Encapsulating Polytungstate Ligand. *J. Am. Chem. Soc.* **2005**, *127* (34), 11948−11949.
(58) Cao, R.; Anderson, T. M.; Piccoli, P. M. B.; Schultz, A. J.; Koetzle, T. F.; Geletii, Y. V.; Slonkina, E.; Hedman, B.; Hodgson, K. O.; Hardcastle, K. I.; Fang, X.; Kirk, M. L.; Knottenbelt, S.; Kögerler, P.; Musaev, D. G.; Morokuma, K.; Takahashi, M.; Hill, C. L. Terminal Gold-Oxo Complexes. *J. Am. Chem. Soc.* **2007**, *129* (36), 11118−11133.
(59) Anh, N. T. In *Frontier Orbitals: A Practical Manual*; Wiley & Sons, Ltd.: New York, 2007; pp 5−24.
(60) Pople, J. A. Molecular orbital perturbation theory II. Charge displacement and stabilization in conjugated molecules. *Proc. R. Soc. Lond. A* **1955**, *233* (1193), 233−241.

DOI: 10.1021/acs.inorgchem.9b03474
Inorg. Chem. 2020, 59, 1556−1565

(61) Libit, L.; Hoffmann, R. Detailed orbital theory of substituent effects. Charge transfer, polarization, and the methyl group. *J. Am. Chem. Soc.* **1974**, *96* (5), 1370−1383.
(62) Hückel, E. Zur Quantentheorie der Doppelbindung. *Eur. Phys. J. A* **1930**, *60* (7−8), 423−456.
(63) Hoffmann, R. An Extended Hückel Theory. I. Hydrocarbons. *J. Chem. Phys.* **1963**, *39* (6), 1397−1412.
(64) Pauling, L. The Nature of the Chemical Bond. Application of Results Obtained from the Quantum Mechanics and from a Theory of Paramagnetic Susceptibility to the Structure of Molecules. *J. Am. Chem. Soc.* **1931**, *53* (4), 1367−1400.
(65) Slater, J. C. Directed Valence in Polyatomic Molecules. *Phys. Rev.* **1931**, *37* (5), 481−489.
(66) Mulliken, R. S. Electronic Structures of Polyatomic Molecules and Valence. II. General Considerations. *Phys. Rev.* **1932**, *41* (1), 49−71.

DOI: 10.1021/acs.inorgchem.9b03474
Inorg. Chem. 2020, 59, 1556−1565

A1.3 “All-electron scalar relativistic basis sets for the elements Rb–Xe”[4]

Received: 14 February 2020 | Revised: 13 May 2020 | Accepted: 18 May 2020

DOI: 10.1002/jcc.26355

FULL PAPER

Journal of COMPUTATIONAL CHEMISTRY WILEY

All-electron scalar relativistic basis sets for the elements Rb–Xe

Julian D. Rolfes | Frank Neese | Dimitrios A. Pantazis

Max-Planck-Institut für Kohlenforschung, Mülheim an der Ruhr, Germany

Correspondence
Frank Neese and Dimitrios A. Pantazis, Max-Planck-Institut für Kohlenforschung, Kaiser-Wilhelm-Platz 1, D-45470 Mülheim an der Ruhr, Germany.
Email: frank.neese@kofo.mpg.de (F. N.) and
Email: dimitrios.pantazis@kofo.mpg.de (D. A. P.)

Funding information
Max Planck Society

Abstract

Segmented all-electron relativistically contracted (SARC) basis sets are presented for the elements $_{37}$Rb–$_{54}$Xe, for use with the second-order Douglas–Kroll–Hess approach and the zeroth-order regular approximation. The basis sets have a common set of exponents produced with established heuristic procedures, but have contractions optimized individually for each scalar relativistic Hamiltonian. Their compact size and loose segmented contraction, which is in line with the construction of SARC basis sets for heavier elements, makes them suitable for routine calculations on large systems and when core spectroscopic properties are of interest. The basis sets are of triple-zeta quality and come in singly or doubly polarized versions, which are appropriate for both density functional theory and correlated wave function theory calculations. The quality of the basis sets is assessed against large decontracted reference basis sets for a number of atomic and ionic properties, while their general applicability is demonstrated with selected molecular examples.

KEYWORDS

basis sets, DKH, scalar relativistic Hamiltonians, ZORA

1 | INTRODUCTION

Consideration of the effects of relativity is an important aspect in the theoretical modeling of chemical systems.[1–7] At the all-electron level, relativistic effects are included in quantum chemical calculations through various levels of approximation to the fully relativistic four-component Dirac Hamiltonian. The latter can be reduced[8,9] exactly or approximately to a quasi-relativistic two-component Hamiltonian following various different formalisms.[5,6] Additionally, spin-dependent terms may be eliminated in these Hamiltonians to provide spin-free scalar relativistic formulations. Among the most popular approximations that have been extensively implemented in quantum chemistry packages and find wide use even in nonspecialist applications of quantum chemistry are the Douglas–Kroll–Hess (DKH) method,[10–16] the zeroth-order regular approximation (ZORA),[17–19] and the exact-2-component approach (X2C).[20–27]

Each quasi-relativistic approach presents distinct requirements with respect to the design and construction of the basis sets used in molecular quantum chemistry calculations, a consideration additional to the appropriateness of a given basis set for the type of electronic structure method and, occasionally, for the targeted property.[28,29] As a result, several families of all-electron basis sets exist and more are being actively developed, that attempt to address these combined requirements in an optimal and balanced way. In recent years, we have been developing a family of segmented all-electron relativistically contracted (SARC)[30–34] basis sets for routine calculations, chiefly based on density functional theory (DFT), in combination with two widely available scalar relativistic Hamiltonians, namely the second-order Douglas–Kroll–Hess (DKH2)[10–16] and the ZORA.[17–19] The construction of the basis sets follows simple rules and strives to provide a reasonable compromise between accuracy and efficiency. The SARC basis sets have already been used extensively in hundreds

of applications and represent the main options for DKH2 and ZORA calculations in the popular ORCA program package.[35,36] The SARC family so far covers elements past Xe and up to Lr.[30–34] For their combination with lighter atoms we proposed Hamiltonian-specific recontractions of all-electron nonrelativistic Karlsruhe basis sets.[37] This was deemed sufficient for elements up to Kr and the corresponding recontracted versions are available in ORCA as DKH-def2- or ZORA-def2-basis sets. However, no satisfying solution existed so far for the elements Rb–Xe, for which recontracted primitives from small nonrelativistic Ahlrichs–May basis sets[38] were used as a temporary solution. These basis sets were very weakly polarized and their construction and range of exponents were far from optimal for use with scalar relativistic Hamiltonians in combination with modern quantum chemical methods. This deficiency is particularly crucial for the chemically important 4*d* transition metals. Here we propose a series of DKH2 and ZORA SARC basis sets developed from the ground up for the fifth-row elements Rb–Xe.

The new basis sets maintain the segmented and loosely contracted design of previous SARC basis sets.[30–34] Exponents were obtained with an even-tempered progression and were contracted individually for the DKH2 and ZORA Hamiltonians and the final set of primitives was adapted to the different requirements of the *s*, *d*, and *p* blocks based on the chemical nature of the included elements. The basis sets are equivalent to triple-zeta quality and can be combined with the other members the SARC family as well as with the recontracted[30] def2 basis sets[37] for elements up to Kr. The generated basis sets are complemented with one set of polarization functions (–P) for methods like DFT as well as with a more extensive set of correlation functions (–PP) for common wave function based post-Hartree–Fock methods. The new SARC basis sets are evaluated for a range of atomic and molecular properties and shown to combine good accuracy while maintaining a reasonable size that facilitates their use in realistic applications. All SARC basis sets are provided in input format as Supporting Information and are included in the basis set library of the ORCA program package.[35]

2 | CONSTRUCTION OF BASIS SETS

Following the well-described procedure for the generation of SARC basis sets,[30–34] the starting point was the determination of the radial expectation values of the innermost orbitals for every angular momentum quantum number. These values were used as generator functions for producing an even-tempered series of primitive Gaussian functions for each angular momentum, as described previously[30–33] and summarized below. The initial radial expectation values were obtained from atomic ground-state restricted open-shell Hartree–Fock (ROHF) calculations, following the Stavrev–Zerner spin-averaged (SA) formalism.[39] The SA-ROHF is a variant of Zerner's configuration-averaged (CA) formalism,[40] that averages over all states with not only a given configuration, but also a given spin, which leads to the production of degenerate orbitals. Exponents from the universal Gaussian basis set (UGBS) by de Castro and Jorge[41] were utilized to generate a sufficiently large, completely decontracted (29*s*21*p*17*d*) basis set as reference for benchmark calculations. In the following, "UGBS" refers to this extended basis set, comprising 177 functions per atom. For the assessment of the innermost radial expectation values $\langle r_l \rangle$, as well as for property calculations, the DKH2 scalar relativistic Hamiltonian was employed.

All atoms were considered in their atomic ground states. These are the following, including their atomic valence electron configurations: Rb (^{2}S, $5s^1$), Sr (^{1}S, $5s^2$), Y (^{2}D, $4d^15s^2$), Zr (^{3}F, $4d^25s^2$), Nb (^{6}D, $4d^45s^1$), Mo (^{7}S, $4d^55s^1$), Tc (^{6}S, $4d^55s^2$), Ru (^{5}F, $4d^75s^1$), Rh (^{4}F, $4d^85s^1$), Pd (^{1}S, $4d^{10}$), Ag (^{2}S, $4d^{10}5s^1$), Cd (^{1}S, $4d^{10}5s^2$), In (^{2}P, $4d^{10}5s^25p^1$), Sn (^{3}P, $4d^{10}5s^25p^2$), Sb (^{4}S, $4d^{10}5s^25p^3$), Te (^{3}P, $4d^{10}5s^25p^4$), I (^{2}P, $4d^{10}5s^25p^5$), and Xe (^{1}S, $4d^{10}5s^25p^6$). The resulting innermost radial expectation values $\langle r_l \rangle$ for the 1*s*, 2*p*, and 3*d* orbitals are listed in Table 1.

From the SA-ROHF/UGBS radial expectation values, we derived the generator exponents α_l of the tightest *s*, *p*, and *d* functions following a previously described procedure according to:

$$\alpha_l = k_l \frac{2 {f_l}^2}{\pi \langle r_l \rangle^2}$$

The factor f_l is 1, 4/3, and 8/5 for l = *s*, *p*, and *d*, and k_l is an empirically adjustable scaling factor that defines the magnitude of the tightest exponent for each angular momentum. For the present case of the elements Rb–Xe, k_l was set to 2000, 250, and 50 for *s*, *p*, and *d* functions, respectively. These values were found in test atomic calculations to produce exponents sufficiently high to be appropriate for

TABLE 1 Radial expectation values of innermost orbitals (in Bohr) determined from spin-averaged DKH2-ROHF calculations with the UGBS basis set

Element	$\langle r_s \rangle$	$\langle r_p \rangle$	$\langle r_d \rangle$
Rb	0.039830	0.154925	0.522941
Sr	0.038688	0.150204	0.496413
Y	0.037603	0.145748	0.472567
Zr	0.036571	0.141537	0.451126
Nb	0.035588	0.137550	0.431615
Mo	0.034650	0.133770	0.413899
Tc	0.033755	0.130180	0.397817
Ru	0.032898	0.126767	0.382946
Rh	0.032079	0.123518	0.369255
Pd	0.031293	0.120421	0.356409
Ag	0.030540	0.117467	0.344603
Cd	0.029817	0.114644	0.333575
In	0.029122	0.111943	0.323245
Sn	0.028453	0.109358	0.313544
Sb	0.027810	0.106880	0.304413
Te	0.027189	0.104503	0.295800
I	0.026591	0.102221	0.287664
Xe	0.026014	0.100027	0.279964

the scalar ZORA and DKH2 relativistic Hamiltonians, without being so high as to create the potential for grid-related numerical instabilities in DFT calculations.[28] As discussed previously,[30–33] keeping these values constant across a row of the periodic table is a pragmatic choice to enable straightforward construction of a complete basis set family, in line with the philosophy of simplicity followed in the construction of the SARC basis sets. The resulting maximum exponents are given in Table 2.

Subsequently, the basis set primitives were constructed in an even-tempered fashion using the series $\alpha_l \cdot \chi_l^{-i}$ (i = 1, 2, 3, …) with the parameter χ_l set to 2.25, 2.50, and 2.80 for l = *s*, *p*, and *d*, respectively. This parameter controls the spacing of one primitive function from the next one, that is, the ratio between successive Gaussian exponents. The termination of the series is controlled by a cutoff value σ set individually for every atom to $\sigma = Z \cdot n_l$ with Z being the atomic number and n_l (l = *s*, *p*, and *d*) being a cutoff parameter calibrated individually for the *s*, *p*, and *d* block elements (see Table 3). This defines the most diffuse exponent for each angular momentum. Collectively, therefore, the above parameters define the total number of primitive functions that are generated for each angular momentum. The above values were selected empirically by a combination of testing with respect to atomic properties for selected elements relative to the UGBS reference and by taking into account approximate target sizes for each angular momentum subspace. The latter approximate targets are used as an important constraint because we require the new basis sets to be compatible in usage with the existing SARC basis sets for elements heavier than Xe and with the recontracted def2 all-electron basis sets for elements lighter than Rb, and hence intermediate in size.

TABLE 2 Maximum exponents per angular momentum α_l (in Bohr^{-2}) used in the SARC basis sets

Element	α_s	α_p	α_d
Rb	802,582.167241	11,788.392711	297.978347
Sr	850,663.033114	12,541.070472	330.676856
Y	900,461.459177	13,319.637239	364.891134
Zr	951,998.900662	14,123.997520	400.400284
Nb	1,005,316.833948	14,954.655585	437.418386
Mo	1,060,482.828479	15,811.757705	475.665155
Tc	1,117,464.908547	16,695.870613	514.900622
Ru	1,176,443.639667	17,606.992511	555.667527
Rh	1,237,281.375224	18,545.438347	597.636788
Pd	1,300,216.635828	19,511.611774	641.494250
Ag	1,365,123.846655	20,505.286897	686.202008
Cd	1,432,129.293106	21,527.566722	732.323723
In	1,501,300.826074	22,578.948957	779.877626
Sn	1,572,729.347489	23,659.005588	828.882754
Sb	1,646,296.826083	24,768.785640	879.353917
Te	1,722,358.882847	25,908.369888	931.308900
I	1,800,697.570348	27,078.048041	984.734293
Xe	1,881,463.713587	28,278.939416	1,039.646541

From the resulting uncontracted basis set, which is the same for both scalar relativistic Hamiltonians, the innermost eight *s*, six *p*, and five *d* functions where then contracted to contracted Gaussian-type functions (CGTFs). This was found to be the maximum acceptable number of contracted primitives that results in acceptable contraction errors compared to the UGBS reference. In line with the existing SARC basis sets, no other contraction is employed. An augmented diffuse function of *p* type is added for the valence space of the 5*p* block elements to account for their potential (partially) anionic character in molecular and ionic calculations. Contraction coefficients were optimized for ZORA and DKH2 scalar relativistic Hamiltonians separately in order to account for the differences in relativistic treatment of the innermost electrons by the two approximations.[28] An example of the differences produced by the two Hamiltonians on the *s* orbitals of Cadmium is provided in Figure S1 of the Supporting Information. In view of the number of functions used to describe the valence space of the neutral and most common ionic configurations of the elements, the resulting SARC basis sets can be considered of triple-ζ quality, although the highly uncontracted nature of the basis sets makes this nomenclature rather imprecise. The utilization of five *d* functions for Y–Cd formally exceeds the triple-ζ designation but is in line with other recently proposed all-electron basis sets for these elements.[42] The cutoff parameters n_l, as well as the final size and contraction pattern of the new SARC basis sets are summarized in Table 3.

As additional polarization functions, we opted for a conservative DFT-oriented approach in the definition of SARC-TZVP. For *d* block elements, scaling the sum of the two most diffuse *d* functions by 1.93 generated a set of *f* functions, while for *p* block elements the outermost *d* function was scaled by 1.43 to generate a set of *f* primitives. Additional polarization/correlation functions (SARC-TZVPP) were generated as follows, guided by maximizing the correlation energy recovered in test CCSD(T) calculations: for *s* block elements, an additional set of *f* primitives was generated by scaling the sum of the last two *d* functions by 1.59. For *p* block elements, two sets of *f* primitives were generated by scaling the average of the two most diffuse *d* functions by 0.69 and 4.41. For *d* block elements, the sum of the two outer *d* functions was scaled by 0.98 and 3.48 for two sets of *f* primitives and 2.13 for an extra set of *g* primitives. The *d* block elements were additionally augmented with a diffuse *d* primitive, consecutively following the generation procedure described above. For optimal balance, the combination of the presented basis sets is recommended with the already published SARC basis sets for heavier elements and the ZORA or DKH2 recontracted all-electron def2-TZVP basis sets for lighter elements in molecular calculations.

3 | ASSESSMENT OF BASIS SETS

In this section, the performance of the new SARC basis sets is assessed for selected properties. Atomic properties were calculated without additional polarization functions (SARC-TZV) to enable direct comparison and evaluation of incompleteness errors against the large

TABLE 3 Cutoff parameters n_l for *s*, *p* and *d* block elements, used in the generation of the SARC basis sets, and the resulting size (number of functions) and pattern of the corresponding uncontracted (U-SARC) and (contracted) SARC basis sets

Elements	n_s	n_p	n_d	U-SARC size	SARC-TZV size
s block	0.0018	0.0018	0.005	112 (22*s*15*p*9*d*)	70 [15*s*10*p*5*d*]
d block	0.0018	0.0018	0.005	112 (22*s*15*p*9*d*)	70 [15*s*10*p*5*d*]
p block	0.0018	0.0010	0.005	115 (22*s*16*p*9*d*)	73 [15*s*11*p*5*d*]

TABLE 4 Estimated incompleteness and contraction errors (E_h) from comparison of the UGBS with uncontracted (U-SARC) and contracted SARC-TZV basis sets using spin-averaged ROHF calculations with the DKH2 Hamiltonian

Element	UGBS	U-SARC	SARC	ΔE_{incomp}	$\Delta E_{contr.}$
Rb	−2,978.882826	−2,978.807987	−2,978.801387	0.074839	0.006600
Sr	−3,177.042664	−3,176.959874	−3,176.952455	0.082790	0.007420
Y	−3,382.596729	−3,382.503930	−3,382.495565	0.092799	0.008365
Zr	−3,595.790955	−3,595.687277	−3,595.677825	0.103678	0.009452
Nb	−3,816.829093	−3,816.712366	−3,816.701612	0.116727	0.010754
Mo	−4,045.740938	−4,045.610935	−4,045.598771	0.130003	0.012164
Tc	−4,282.473586	−4,282.329671	−4,282.315980	0.143915	0.013691
Ru	−4,527.359444	−4,527.198159	−4,527.182679	0.161285	0.015480
Rh	−4,780.464841	−4,780.285780	−4,780.268289	0.179061	0.017491
Pd	−5,041.903747	−5,041.702055	−5,041.682252	0.201692	0.019803
Ag	−5,311.865066	−5,311.645843	−5,311.623497	0.219223	0.022346
Cd	−5,590.255633	−5,590.015344	−5,589.990086	0.240289	0.025258
In	−5,877.040384	−5,876.780360	−5,876.751755	0.260024	0.028605
Sn	−6,172.404077	−6,172.117660	−6,172.085350	0.286417	0.032310
Sb	−6,476.450405	−6,476.136315	−6,476.100013	0.314090	0.036302
Te	−6,789.178209	−6,788.835449	−6,788.794887	0.342760	0.040562
I	−7,110.789125	−7,110.415776	−7,110.370708	0.373349	0.045068
Xe	−7,441.394819	−7,440.988867	−7,440.939047	0.405952	0.049820

UGBS reference. Molecular properties were calculated with the inclusion of polarization functions for transition metals (SARC-TZVP), while all post-Hartree–Fock calculations reported here were performed with additional correlation functions (SARC-TZVPP). Lighter elements were equipped with relativistically recontracted def2-TZVP basis sets for Hartree–Fock and DFT, and with relativistically recontracted def2-TZVPP basis sets for correlated wave function based methods.

3.1 | Atomic properties

The assessment of the internal consistency and construction quality of the newly generated SARC basis sets began with SAHF calculations of the atomic ground states. The resulting energies were compared to energies obtained with the fully uncontracted SARC (U-SARC) basis sets as well as the UGBS basis sets in order to determine both the estimated incompleteness error and the contraction error. All ground state absolute energy values for the fifth period elements and incompleteness and contraction errors are given in Table 4. Both errors rise monotonically, the latter between 6.6 mE_h for Rubidium and 50 mE_h for Xenon and the former between 75 mE_h for Rubidium and 406 mE_h for Xenon. The overall deviation of the total energy from the values obtained with UGBS basis sets stays below 0.5 E_h for the whole SARC series, which compares very favorably with corresponding values for heavier elements. As an indication of the impact on the computational cost, the total run time for the calculation of the Rh ground state energy on 1 CPU is reduced from 5 min and 4 s (UGBS) to 23 s (U-SARC) and the consecutive introduction of contraction reduces the run time further down to 11 s (SARC).

A more detailed measure of basis set performance for atomic systems is found by comparison of all orbital energies and radial expectation values between the results obtained with UGBS basis set and the results obtained with the newly generated SARC basis set. Xenon was chosen as a representative example, because the proper representation of its innermost orbitals has the highest requirements on the CGTFs, and hence the biggest deviation in the energies of the innermost orbitals from the values obtained with the UGBS basis set was expected—and observed—for Xenon. The deviation in the calculated orbital energies for Xenon does not exceed 71 mE_h and practically disappears in the valence region. The radial expectation values are in extremely good agreement, with practically identical results in the core region and deviations in the valence region staying well below 0.1 pm (0.0019 Bohr). All orbital energies and radial expectation

TABLE 5 Orbital energies (E_h) and radial expectation values (Bohr) for Xenon: Comparison between UGBS and SARC-TZV basis sets from HF calculations with the DKH2 Hamiltonian

	UGBS		SARC			
	E	⟨*r*⟩	*E*	⟨*r*⟩	Δ*E*	Δ⟨*r*⟩
1*s*	−1,275.1970	0.0260	−1,275.2533	0.0260	−0.0563	0.0000
2*s*	−202.2477	0.1139	−202.3150	0.1139	−0.0673	0.0000
2*p*	−181.4455	0.1000	−181.517	0.1000	−0.0711	0.0000
3*s*	−42.9723	0.3047	−43.0106	0.3047	−0.0382	0.0000
3*p*	−36.0620	0.3028	−36.0943	0.3029	−0.0324	0.0001
3*d*	−25.7330	0.2800	−25.7613	0.2801	−0.0283	0.0001
4*s*	−8.4230	0.7175	−8.4371	0.7172	−0.0141	−0.0003
4*p*	−6.1322	0.7647	−6.1406	0.7647	−0.0084	0.0000
4*d*	−2.6659	0.8762	−2.6645	0.8778	0.0015	0.0016
5*s*	−1.0090	1.9058	−1.0102	1.9047	−0.0012	−0.0012
5*p*	−0.4563	2.3139	−0.4566	2.3142	−0.0002	0.0003

TABLE 6 B3LYP-DKH2 results with the SARC-TZV and UGBS basis sets for the first, second, and third ionization potentials (in eV) for Rb–Xe

	UGBS			SARC			Expt.[45]		
Element	IP_1	IP_2	IP_3	IP_1	IP_2	IP_3	IP_1	IP_2	IP_3
Rb	4.26	27.41	–	4.24	27.41	–	4.18	27.29	–
Sr	5.68	11.20	–	5.68	11.20	–	5.69	11.03	–
Y	6.30	12.24	20.70	6.30	12.25	20.71	6.22	12.24	20.52
Zr	6.51	13.22	23.32	6.49	13.23	23.31	6.63	13.13	22.99
Nb	6.84	14.25	25.29	6.78	14.24	25.29	6.76	14.32	25.04
Mo	7.15	16.18	27.16	7.11	16.17	27.15	7.09	16.16	27.13
Tc	7.03	15.30	29.75	7.15	15.31	29.73	7.28	15.26	29.54
Ru	7.51	16.96	28.56	7.47	16.95	28.56	7.36	16.76	28.47
Rh	7.63	18.31	31.21	7.59	18.30	31.20	7.46	18.08	31.06
Pd	8.64	19.62	33.10	8.44	19.62	33.09	8.34	19.43	32.93
Ag	7.81	21.76	34.94	7.77	21.75	34.93	7.58	21.49	34.83
Cd	8.99	17.26	37.71	8.99	17.28	37.70	8.99	16.91	37.48
In	5.57	18.94	–	5.57	18.95	–	5.79	18.87	–
Sn	7.19	14.23	–	7.20	14.24	–	7.34	14.63	–
Sb	8.86	16.43	–	8.87	16.44	–	8.61	16.53	–
Te	8.77	18.67	–	8.77	18.68	–	9.01	18.60	–
I	10.55	18.76	–	10.55	18.78	–	10.45	19.13	–
Xe	12.40	21.11	–	12.41	21.12	–	12.13	21.21	–

values for Xenon with UGBS and SARC basis sets as well as their differences are given in Table 5 (see Supporting Information Table S2 for corresponding B3LYP orbital energies).

The representation of the valence orbitals is a good indicator of the accuracy of a given basis set, but ionization potentials (IPs) and electron affinities (EAs) calculated at the DFT level give a more detailed insight into the practical applicability of the new SARC basis sets. Comparison of the first two IPs for all fifth period elements and additional third IP for second row transition metals calculated with the B3LYP functional[43,44] show an overall good agreement between the values calculated with UGBS and SARC basis sets (Table 6). Most of the deviations lie below 0.05 eV, never exceeding 0.20 eV. The experimental values are provided for reference, but we note that the better agreement in some cases of the IPs calculated with SARC basis sets with experiment compared to those calculated with UGBS basis sets should not be read as more than accidental, given that the complete basis set limit of the method might still not be captured by UGBS and that the experimental values incorporate effects that are ignored in the present calculations, such as spin–orbit coupling.

Due to the increase in electronegativity, EAs, which require a proper electronic description of anionic states, become increasingly important down the row. Hence, *p* block elements were equipped with an additional diffuse *p* function to account for this requirement. The resulting EA values, in analogy to the IP values given above, can

TABLE 7 B3LYP-DKH2 electron affinities (in eV) for In–I with the UGBS and SARC-TZV basis sets

Element	UGBS	SARC	Expt.[46–50]
In	0.24	0.34	0.38
Sn	1.22	1.26	1.11
Sb	0.94	0.97	1.05
Te	2.06	2.07	1.97
I	3.27	3.28	3.06

be found in Table 7. Again, most of the deviations between the results obtained with SARC and UGBS basis sets lie below 0.05 eV.

All the above examples are reported with the DKH2 Hamiltonian. Supporting Information Tables S1, S3, and S4 provide the corresponding ZORA versions of Tables 5, 6, and 7. The ZORA results are perfectly in line with the conclusions drawn above on the basis of the DKH2 calculations.

To analyze how the newly generated SARC basis sets perform with post-Hartree–Fock methods, the EA of iodine was also assessed through CCSD(T) calculations with the SARC basis set, augmented with the correlation functions introduced above, as well as with the corresponding DKH-optimized basis sets from the correlation-consistent basis set family.[51] The calculation with the DKH2 version of SARC-TZVPP yielded an EA for iodine of 3.02 eV, while employing the series of cc-pVTZ-DK, aug-cc-pVTZ-DK, and cc-pVQZ-DK basis sets resulted in EA values of 2.91, 3.19, and 3.23 eV, respectively (the reported experimental value[50] is 3.06 eV). Another example that demonstrates the accuracy and efficiency of the newly generated SARC basis set is the calculation of the excitation energy of Zr from its ($4d^2 5s^2$, $S = 1$) ground state to its ($4d^3 5s$, $S = 2$) state (experimental value reported as 5,541 cm^{-1}).[52] The corresponding DKH2 CCSD(T) calculation with SARC-TZVPP yielded an excitation energy of 5,077 cm^{-1} while the same calculation with the cc-pVTZ-DK basis set[53] gave an excitation energy of 4,278 cm^{-1}. The SARC-TZVPP basis sets were found to recover more correlation energy in these calculations compared to the correlation-consistent basis sets, a result that might be in part related to the greater number of uncontracted functions and in part to the tighter exponents for the high angular momentum functions used in the SARC basis sets. We acknowledge that correlated wave function calculations are not the principal domain of intended application for the SARC basis sets. Other basis sets, usually incorporating general contractions, have been proposed specifically for such calculations[51,53–61] and they often also offer the possibility of basis set extrapolation through a systematically converging series. Nevertheless, the above observations suggest that in their TZVPP version the SARC basis sets are sufficiently flexible to be used in routine wave function based calculations.

3.2 | Molecular applications

This section presents selected examples relating to molecular applications and includes comparisons of the SARC basis sets with other basis sets available in the literature. Assessment of molecular properties with the new SARC basis sets starts with representative analyses of basis set superposition error (BSSE) with the counterpoise correction method by Boys and Bernardi.[62] The potential energy surfaces of selected diatomic molecules were scanned using the PBE0 hybrid functional[63] with the DKH2 Hamiltonian. The optimized bond lengths and the dissociation energies of all dimers with and without the counterpoise correction, as well as their differences, are summarized in Table 8. The deviation of dissociation energies with and without CPC is generally found between 0.01 and 0.02 eV, while the deviation in bond length is essentially zero. The comparison leads to the conclusion that there are no significant BSSE effects in the valence space to be expected from the new SARC basis sets in molecular DFT calculations.

TABLE 8 Bond lengths r (Å) and dissociation energies D_e (eV) of strontium, silver, and (homonuclear) iodine diatomics computed with the PBE0 density functional and the DKH2 Hamiltonian, without and with BSSE counterpoise corrections (CPC)

	SARC-TZVP		SARC-TZVP+CPC			
	r	D_e	r	D_e	Δr	ΔD_e
SrH	2.136	1.79	2.136	1.79	0.000	0.00
SrO	1.905	4.06	1.905	4.05	0.000	−0.01
SrF	2.080	5.39	2.080	5.38	0.000	−0.01
AgH	1.623	2.27	1.623	2.26	0.000	−0.01
AgO	1.931	0.76	1.931	0.74	0.000	−0.02
AgF	1.987	3.22	1.987	3.20	0.000	−0.02
I_2	2.663	2.03	2.663	2.02	0.000	−0.01

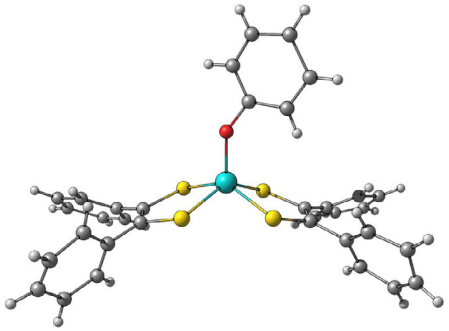

FIGURE 1 Structure of $[Mo^{IV}(OPh)(S_2C_2Ph_2)_2]^-$[64] [Color figure can be viewed at wileyonlinelibrary.com]

As another test case, we use a transition metal complex to compare the effect of the choice of method on geometry optimization. Figure 1 shows the structure of the complex $[Mo^{IV}(OPh)(S_2C_2Ph_2)_2]^-$, a molybdenum system reported by Lim and Holm[64] as a biomimetic analogue for the active site of Mo-containing enzymes that comprises two chelate phenyl-substituted dithiolenes and a phenoxy group.

Crystallographic coordinates of the complex (ID: IDELUY) were used as the starting point for DFT geometry optimizations with the BP86 functional.[65,66] Increased integration grids were applied throughout (Grid6 in ORCA nomenclature). Table 9 compares the Mo–O and Mo–S bond

TABLE 9 Optimized Mo–O and Mo–S (averaged) bond lengths (in Å) for $[Mo^{IV}(OPh)(S_2C_2Ph_2)_2]^-$ using different Mo basis sets and Hamiltonian combinations

Method	Mo–O	Mo–S
Expt.	1.886	2.326
def2-TZVP	1.908	2.327
def2-TZVPP	1.906	2.327
ZORA/SARC-ZORA-TZVP	1.912	2.329
ZORA/SARC-ZORA-TZVPP	1.909	2.328
DKH2/SARC-DKH-TZVP	1.879	2.250
DKH2/SARC-DKH-TZVPP	1.882	2.257

Note: All results were obtained with the BP86 functional and all-electron def2-TZVP basis sets for ligand atoms, either in their nonrelativistic[37] or relativistically recontracted versions as appropriate. The "AutoAux" procedure of ORCA was used for the generation of auxiliary basis sets when needed[67] and the "DKH1CAutoAux" setting was activated for geometry optimizations with the DKH2 Hamiltonian.

lengths obtained with a different basis sets for Mo and different scalar relativistic Hamiltonians, specifically the def2-TZVP and def2-TZVPP basis sets that employ an effective core potential (ECP) replacing the inner 28 electrons of Mo[68] (corresponding valence space contractions are [6*s*4*p*3*d*1*f*] and [6*s*4*p*3*d*2*f*1*g*], respectively),[37] and the new SARC basis sets with the ZORA and the DKH2 approaches. Optimizations that use the ECP basis set for Mo and the SARC-ZORA all-electron calculations provide almost indistinguishable results, approximating the crystallographic parameters equally well. This is a nice indication that the two approaches can be used interchangeably for geometry optimizations. DKH2 calculations provide slightly shorter Mo–O bonds but on the other hand they also yield rather too short Mo–S bond lengths. ZORA calculations proved robust and neither required nor were they affected by further increase in radial integration accuracy. In contrast, this had a beneficial effect on the stability and rate of convergence of DKH2 calculations, albeit increasing at the same time the computational cost. Interestingly, even though the ECP-based calculations had an advantage in terms of the time required to complete the self-consistent-field procedure owing to the smaller total number of basis functions, the ZORA all-electron optimizations either with the SARC-TZVP or the SARC-TZVPP basis sets were always the fastest calculations for the present complex because they consistently required the least optimization steps to converge to the minimum. It is noted that in cases when ZORA turns out to be the preferred all-electron scalar relativistic approach, as for the present system, the SARC basis sets may currently be the only choice for quantum chemistry programs that use Gaussian-type basis sets, as the only other ZORA-specific option known to us are the Slater-type basis sets of Van Lenthe and Baerends.[69]

A different type of application concerns the analysis of valence orbitals in transition metal complexes on the basis of multireference calculations. As a test case, we use the $MoOCl_5^{2-}$ complex and demonstrate the results of ab initio ligand field theory (AILFT) analysis[70] of its *d* manifold based on complete active space SCF (CASSCF) calculations. Table 10 summarizes the results obtained using the SARC basis sets for Mo (CASSCF calculation with the DKH2 Hamiltonian) and compares the produced values to those obtained with the standard ECP-based def2-TZVP and def2-TZVPP basis

TABLE 10 Comparison of basis sets for the ab initio ligand field theory (AILFT) analysis of the *d* manifold of $MoOCl_5^{2-}$ (energies relative to d_{xy} in cm^{-1}) from CASSCF calculations

Mo basis set	d_{xy}	d_{xz}/d_{yz}	$d_{x^2-y^2}$	d_{z^2}
def2-TZVP	0	14,300	22,290	45,290
def2-TZVPP	0	14,290	22,180	45,270
SARC-DKH-TZVP	0	14,160	22,010	44,840
SARC-DKH-TZVPP	0	14,150	22,000	44,770
Sapporo-DKH-TZP	0	14,130	21,840	44,760
cc-pVTZ-DK	0	14,150	21,920	44,750
Jorge-TZP-DKH	0	15,260	33,230	31,760
Expt.[71]	0	13,800	23,000	–

sets[37,68] as well as with the all-electron Jorge-TZP-DKH,[60] Sapporo-DKH-TZP-2012,[61] and cc-pVTZ-DK[53] basis sets.

The results suggest that the valence description is very similar at the CASSCF level between the new all-electron SARC basis sets and the ECP-based def2 basis sets. Among the all-electron basis sets, the results obtained with the SARC, the Sapporo, and the correlation-consistent basis sets almost coincide, albeit the partial incorporation of generally contracted functions in the cc-pVTZ-DK basis set may be associated with higher computational cost depending on the integral code employed. On the other hand, the deviating results and inverted order of the two highest orbitals obtained with the Jorge-TZP-DKH basis set are indicative of a deficiency in the description of the *d* space in its default form. We confirm that this is corrected in the QZP version of the Jorge basis set, which increases the number of *d* functions by one compared to the TZP version but also extends the high angular momentum functions up to *h*.

In summary, although the above examples are by necessity limited, they demonstrate that the SARC basis sets perform reliably in typical molecular applications in conjunction with the ZORA and DKH2 Hamiltonians. In comparison to DKH-optimized all-electron basis sets that employ an analogous segmented contraction the SARC are equal or better than existing alternatives, while also offering the option of a ZORA-specific version that can be useful for many types of calculation. Finally, it is noted that since the SARC basis sets are loosely contracted, they retain considerable flexibility in the core region even in their standard form. This can be important for calculations of spectroscopic parameters that depend on a flexible description of the inner-shell electronic structure or the distribution of electronic or spin density close to the nucleus, such as hyperfine couplings, Mössbauer, and X-ray spectroscopy. For the most physically consistent approach to the description of the core region the use of a finite nucleus model should also be considered.

4 | CONCLUSIONS

We presented a series of SARC basis sets for the elements Rb–Xe. The new basis sets extend the SARC family of ZORA- and DKH2-adapted basis sets to cover the 5*s*, 4*d*, and 5*p* block elements. In keeping with their heavier-element congeners, the new basis sets adopt a loose contraction and utilize a common set of exponents for

both Hamiltonians, with the CGTFs optimized separately for each Hamiltonian. Compared to a large reference basis set, the SARC basis sets were shown to perform consistently across the series and are associated with small incompleteness and contraction errors. Calculations of ionization energies and EAs confirmed that the new basis sets perform reliably for atomic properties. Selected molecular examples indicated that the SARC basis sets are robust and either compare very favorably with existing ECP-based and all-electron alternatives or outperform them while offering increased flexibility, and are hence expected to be a reliable choice for practical applications that utilize the DKH2 or ZORA approaches.

ACKNOWLEDGMENTS

Support by the Max Planck Society is gratefully acknowledged. We thank Georgi Stoychev and Maurice van Gastel for fruitful discussions.

ORCID

Dimitrios A. Pantazis https://orcid.org/0000-0002-2146-9065

REFERENCES

[1] J. Autschbach, *J. Chem. Phys.* **2012**, *136*, 150902.
[2] P. Pyykkö, *Annu. Rev. Phys. Chem.* **2012**, *63*, 45.
[3] K. G. Dyall, K. Faegri Jr.., *Introduction to Relativistic Quantum Chemistry*, Oxford University Press, Oxford **2007**.
[4] M. Reiher, A. Wolf, *Relativistic Quantum Chemistry: The Fundamental Theory of Molecular Science*, Wiley-VCH, Weinheim **2009**.
[5] W. Liu, *Mol. Phys.* **2010**, *108*, 1679.
[6] T. Saue, *ChemPhysChem* **2011**, *12*, 3077.
[7] P. Tecmer, K. Boguslawski, D. Kędziera, in *Handbook of Computational Chemistry* (Ed: J. Leszczynski), Springer, Dordrecht, Netherlands **2016**, p. 1.
[8] L. L. Foldy, S. A. Wouthuysen, *Phys. Rev.* **1950**, *78*, 29.
[9] J. L. Heully, I. Lindgren, E. Lindroth, S. Lundqvist, A. M. Martensson-Pendrill, *J. Phys. B: At., Mol.* **1986**, *19*, 2799.
[10] M. Reiher, *WIREs Comput. Mol. Sci.* **2012**, *2*, 139.
[11] M. Reiher, *Theor. Chem. Acc.* **2006**, *116*, 241.
[12] M. Reiher, A. Wolf, *J. Chem. Phys.* **2004**, *121*, 10945.
[13] C. van Wüllen, *J. Chem. Phys.* **2004**, *120*, 7307.
[14] A. Wolf, M. Reiher, B. A. Hess, *J. Chem. Phys.* **2002**, *117*, 9215.
[15] T. Nakajima, K. Hirao, *J. Chem. Phys.* **2000**, *113*, 7786.
[16] M. Douglas, N. M. Kroll, *Ann. Phys.* **1974**, *82*, 89.
[17] E. van Lenthe, E. J. Baerends, J. G. Snijders, *J. Chem. Phys.* **1993**, *99*, 4597.
[18] E. van Lenthe, E. J. Baerends, J. G. Snijders, *J. Chem. Phys.* **1994**, *101*, 9783.
[19] C. van Wüllen, *J. Chem. Phys.* **1998**, *109*, 392.
[20] W. Kutzelnigg, W. Liu, *J. Chem. Phys.* **2005**, *123*, 241102.
[21] W. Kutzelnigg, W. Liu, *Mol. Phys.* **2006**, *104*, 2225.
[22] W. Liu, D. Peng, *J. Chem. Phys.* **2006**, *125*, 044102.
[23] W. Liu, W. Kutzelnigg, *J. Chem. Phys.* **2007**, *126*, 114107.
[24] M. Iliaš, T. Saue, *J. Chem. Phys.* **2007**, *126*, 064102.
[25] D. Peng, W. Liu, Y. Xiao, L. Cheng, *J. Chem. Phys.* **2007**, *127*, 104106.
[26] W. Liu, D. Peng, *J. Chem. Phys.* **2009**, *131*, 031104.
[27] D. Peng, M. Reiher, *Theor. Chem. Acc.* **2012**, *131*, 1081.
[28] D. A. Pantazis, F. Neese, *WIREs Comput. Mol. Sci.* **2014**, *4*, 363.
[29] J. G. Hill, *Int. J. Quantum Chem.* **2013**, *113*, 21.
[30] D. A. Pantazis, X. Y. Chen, C. R. Landis, F. Neese, *J. Chem. Theory Comput.* **2008**, *4*, 908.
[31] D. A. Pantazis, F. Neese, *J. Chem. Theory Comput.* **2009**, *5*, 2229.
[32] D. A. Pantazis, F. Neese, *J. Chem. Theory Comput.* **2011**, *7*, 677.
[33] D. A. Pantazis, F. Neese, *Theor. Chem. Acc.* **2012**, *131*, 1292.
[34] D. Aravena, F. Neese, D. A. Pantazis, *J. Chem. Theory Comput.* **2016**, *12*, 1148.
[35] F. Neese, *WIREs Comput. Mol. Sci.* **2018**, *8*, e1327.
[36] F. Neese, *WIREs Comput. Mol. Sci.* **2012**, *2*, 73.
[37] F. Weigend, R. Ahlrichs, *Phys. Chem. Chem. Phys.* **2005**, *7*, 3297.
[38] R. Ahlrichs, K. May, *Phys. Chem. Chem. Phys.* **2000**, *2*, 943.
[39] K. K. Stavrev, M. C. Zerner, *Int. J. Quantum Chem.* **1997**, *65*, 877.
[40] M. C. Zerner, *Int. J. Quantum Chem.* **1989**, *35*, 567.
[41] E. V. R. de Castro, F. E. Jorge, *J. Chem. Phys.* **1998**, *108*, 5225.
[42] P. Pollak, F. Weigend, *J. Chem. Theory Comput.* **2017**, *13*, 3696.
[43] A. D. Becke, *J. Chem. Phys.* **1993**, *98*, 5648.
[44] C. Lee, W. Yang, R. G. Parr, *Phys. Rev. B* **1988**, *37*, 785.
[45] D. R. Lide, *CRC Handbook of Chemistry and Physics*, 90th edition CRC Press, Boca Raton, FL **2009**, p. 2804.
[46] C. W. Walter, N. D. Gibson, D. J. Carman, Y. G. Li, D. J. Matyas, *Phys. Rev. A* **2010**, *82*, 032507.
[47] M. Vandevraye, C. Drag, C. Blondel, *J. Phys. B: At., Mol. Opt. Phys.* **2013**, *46*, 125002.
[48] M. Scheer, H. K. Haugen, D. R. Beck, *Phys. Rev. Lett.* **1997**, *79*, 4104.
[49] G. Haeffler, A. E. Klinkmüller, J. Rangell, U. Berzinsh, D. Hanstorp, *Z. Phys. D: At, Mol. Clust.* **1996**, *38*, 211.
[50] R. J. Peláez, C. Blondel, C. Delsart, C. Drag, *J. Phys. B: At., Mol. Opt. Phys.* **2009**, *42*, 125001.
[51] D. H. Bross, K. A. Peterson, *Theor. Chem. Acc.* **2014**, *133*, 1434.
[52] E. Biemont, N. Grevesse, P. Hannaford, R. M. Lowe, *Astrophys. J.* **1981**, *248*, 867.
[53] K. A. Peterson, D. Figgen, M. Dolg, H. Stoll, *J. Chem. Phys.* **2007**, *126*, 124101.
[54] K. A. Peterson, C. Puzzarini, *Theor. Chem. Acc.* **2005**, *114*, 283.
[55] B. O. Roos, R. Lindh, P.-Å. Malmqvist, V. Veryazov, P.-O. Widmark, *J. Phys. Chem. A* **2004**, *108*, 2851.
[56] B. O. Roos, R. Lindh, P.-Å. Malmqvist, V. Veryazov, P.-O. Widmark, *J. Phys. Chem. A* **2005**, *109*, 6575.
[57] K. G. Dyall, *Theor. Chem. Acc.* **2006**, *115*, 441.
[58] K. G. Dyall, *Theor. Chem. Acc.* **2007**, *117*, 483.
[59] K. G. Dyall, *J. Phys. Chem. A* **2009**, *113*, 12638.
[60] C. T. Campos, F. E. Jorge, *Mol. Phys.* **2013**, *111*, 167.
[61] T. Noro, M. Sekiya, T. Koga, *Theor. Chem. Acc.* **2012**, *131*, 1124.
[62] S. F. Boys, F. Bernardi, *Mol. Phys.* **1970**, *19*, 553.
[63] C. Adamo, V. Barone, *J. Chem. Phys.* **1999**, *110*, 6158.
[64] B. S. Lim, R. H. Holm, *J. Am. Chem. Soc.* **2001**, *123*, 1920.
[65] J. P. Perdew, *Phys. Rev. B* **1986**, *33*, 8822.
[66] A. D. Becke, *Phys. Rev. A* **1988**, *38*, 3098.
[67] G. L. Stoychev, A. A. Auer, F. Neese, *J. Chem. Theory Comput.* **2017**, *13*, 554.
[68] D. Andrae, U. Haussermann, M. Dolg, H. Stoll, H. Preuss, *Theor. Chim. Acta* **1990**, *77*, 123.
[69] E. Van Lenthe, E. J. Baerends, *J. Comput. Chem.* **2003**, *24*, 1142.
[70] M. Atanasov, D. Ganyushin, K. Sivalingam, F. Neese, *Struct. Bonding* **2012**, *143*, 149.
[71] H. B. Gray, C. R. Hare, *Inorg. Chem.* **1962**, *1*, 363.

SUPPORTING INFORMATION

Additional supporting information may be found online in the Supporting Information section at the end of this article.

How to cite this article: Rolfes JD, Neese F, Pantazis DA. All-electron scalar relativistic basis sets for the elements Rb–Xe. *J Comput Chem*. 2020;41:1842–1849. https://doi.org/10.1002/jcc.26355